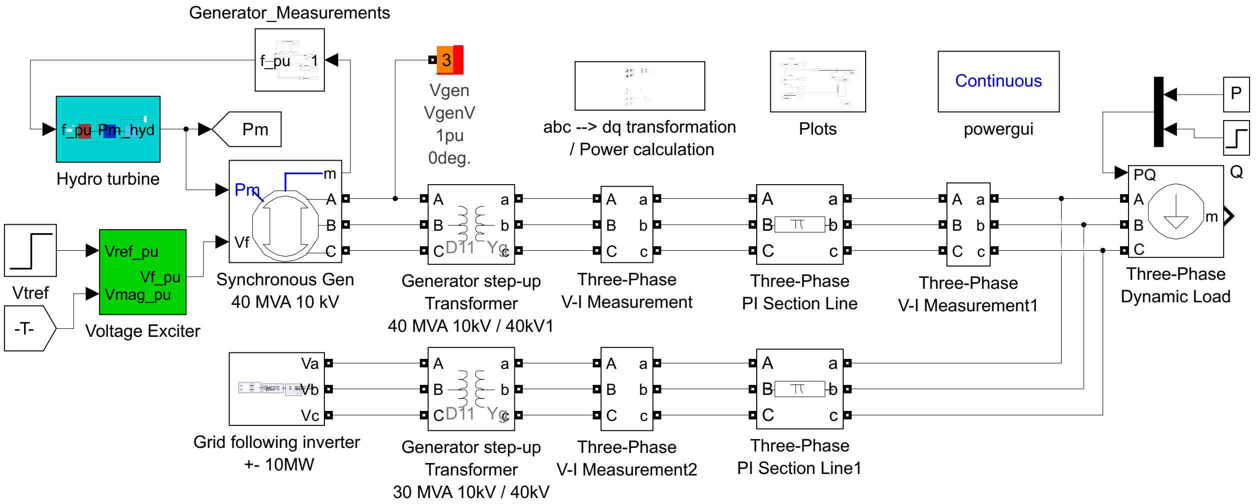

Implementation and Stability Analysis of Synthetic Inertia for Inverter-Based Energy Resources

Master's thesis in Electric Power Engineering

Arvid Karlsson

Carl-Johan Vickström

DEPARTMENT OF ELECTRICAL ENGINEERING

Chalmers University of Technology
Gothenburg, Sweden 2025
www.chalmers.se

Master's thesis 2025

Implementation and Stability Analysis of Synthetic Inertia for Inverter-Based Energy Resources

Arvid Karlsson
Carl-Johan Vickström

Department of Electrical Engineering
Division of Electric Power Engineering
Chalmers University of Technology
Gothenburg, Sweden 2025

Implementation and Stability Analysis of Synthetic Arvid Karlsson, Carl-Johan Vickström

Supervisor: Bengt Johansson, Solvina
Examiner: Peiyuan Chen, Department of Electrical Engineering

Master's Thesis 2025
Department of Electrical Engineering
Division of Electric Power Engineering
Chalmers University of Technology
SE-412 96 Gothenburg
Telephone +46 31 772 1000

Cover: Built grid model in Matlab/Simulink featuring an inverter and synchronous generator supplying a dynamic load.

Typeset in LaTeX
Printed by Chalmers Reproservice
Gothenburg, Sweden 2025

Implementation and Stability Analysis of Synthetic Inertia for Inverter-Based Energy Resources

Arvid Karlsson, Carl-Johan Vickström
Department of Electric Power Engineering
Chalmers University of Technology

Abstract

Inverters are being integrated into power systems around the world at a rapid pace due to the shift from traditional energy sources to renewable sources such as wind and solar power. As the number of inverters increases, the inertia in the system with respect to the power level decreases. Since frequency stability in power systems heavily relies on the kinetic energy stored in rotating masses to provide inertia, such as synchronous generators which are now being partly phased out, it may become necessary for inverters to provide synthetic inertia as well.

This thesis work includes the implementation of grid following and grid forming inverters together with an external grid of variable strength and an island grid constituted of a hydro power generator. The simulations are carried out in Matlab and Simulink. The implementation is based on the theory of existing methods and includes an important definition of synthetic inertia, namely that it is proportional to the rate of change of frequency. Contrary to fast frequency response which is proportional to frequency deviation. The models were then tested against grid frequency disturbances to analyze how aggressively the system could be tuned while still maintaining stability.

The results showed that grid following inverters are highly dependent on the strength of the external grid, mainly because of their need to synchronize their own frequency with the grid. When operating in synthetic inertia mode, the grid following inverter stability region increased linearly between proportional gain and the filtering time constant. When providing active power based on frequency deviation, the stability decreased as the filtering increased. The grid forming inverter was highly dependent on its droop constant to remain stable where as the droop constant increased, the stability decreased.

Keywords: Grid Forming, Grid Following, Synthetic Inertia, FFR, Island Grid, Weak Grid, PLL, Simulink, Virtual Synchronous Machine, RoCoF

Acknowledgements

We would like to thank our supervisor Bengt Johansson for all of his guidance throughout the entire project. Your technical expertise and insightful points have helped to make this thesis what it is today. We would also like to thank our examiner Peiyuan Chen for his dedication to helping us finish this project.

To everyone at Solvina, thank you for making us feel welcomed and included. We are truly grateful for all the help you provided us with when we needed it. Lastly, we want to thank our friends and family who contributed with great energy and cheered us on until the end!

Arvid Karlsson, Carl-Johan Vickström, Gothenburg, June 2025

List of Acronyms

Below is the list of acronyms that have been used throughout this thesis listed in alphabetical order:

BESS	Battery Energy Storage System
EMT	Electromagnetic Transient
FFR	Fast Frequency Response
FRR	Frequency Restoration Reserve
GFL	Grid Following
GFM	Grid Forming
GPS	Global Positioning System
IBR	Inverter Based Resources
PCC	Point of Common Coupling
PLL	Phase Locked Loop
PSC	Power Synchronization Control
PSP	Positive Sequence Phasor
PV	Photovoltaic
RES	Renewable Energy Sources
RoCoF	Rate of Change of Frequency
RMS	Root Mean Square
RPM	Revolution per minute
SCC	Short Circuit Capacity
SG	Synchronous Generator
SRF-PLL	Synchronous Reference Frame Phase Locked Loop
SVK	Svenska Kraftnät
TSO	Transmission System Operator
VCO	Voltage Controlled Oscillator
VSM	Virtual Synchronous Machine
WAMS	Wide Area Monitoring System
ZCD	Zero Crossing Detection

Nomenclature

Below is the nomenclature of indices, sets, parameters, and variables that have been used throughout this thesis.

Variables

H	Inertia constant
D	Damping constant
R	Droop constant
R_{GSU}	Copper resistance of generator step-up transformer (p.u.)
X_{GSU}	Leakage reactance of generator step-up transformer (p.u.)
R_{f}	Filter resistance (Ohm)
L_{f}	Filter inductance (H)
C_{f}	Filter capacitance (F)
T_{ser}	Servo motor time constant (s)
A_{ser}	Servo actuator ramp rate limit (p.u./s)
T_{w}	Water starting time constant (s)
τ	Time constant in ROCOF control (s)
$K_{\mathrm{p,pll}}$	Proportional gain of PLL
$K_{\mathrm{i,pll}}$	Integral gain of PLL
$K_{\mathrm{p,cc}}$	Proportional gain of current controller
$K_{\mathrm{i,cc}}$	Integral gain of current controller
$K_{\mathrm{p,pc}}$	Proportional gain of power controller
$K_{\mathrm{i,pc}}$	Integral gain of power controller
$K_{\mathrm{p,VR}}$	Proportional gain of voltage regulator
$K_{\mathrm{i,VR}}$	Integral gain of voltage regulator
$T_{\mathrm{i,VR}}$	Integration time constant of voltage regulator (s)
$T_{\mathrm{e,VR}}$	Exciter delay time for static exciter (s)

$T_{\mathrm{e,brushless}}$	Exciter delay time for brushless exciter (s)
E_{max}	Maximum exciter output voltage (p.u.)
E_{min}	Minimum exciter output voltage (p.u.)
V_{fd0}	Initial exciter voltage (p.u.)
$V_{\mathrm{g,ref}}$	Generator terminal voltage reference (p.u.)
S_{b}	Base apparent power (VA)
$V_{\mathrm{b,LL,rms}}$	Base line-to-line RMS voltage (V)
V_{b}	Base phase voltage (peak, V)
I_{b}	Base current (phase peak, A)
Z_{b}	Base impedance (Ohm)
f_{n}	Nominal grid frequency (Hz)
f_{sw}	Switching frequency (Hz)
ω_{n}	Nominal angular frequency (rad/s)
S_{gen}	Total power rating of hydro generator (VA)
V_{gen}	Generator voltage level (kV)
V_{grid}	Grid voltage level (kV)
R_1, L_1, C_1	Line positive-sequence resistance (Ohm/km), inductance (H/km), and capacitance (F/km)
R_0, L_0, C_0	Line zero-sequence resistance (Ohm/km), inductance (H/km), and capacitance (F/km)
X_d, X_{d1}, X_{d2}	Generator reactances (p.u.)
$P_{\mathrm{m,init}}$	Initial mechanical power input (p.u.)
$V_{\mathrm{f,init}}$	Initial field voltage (p.u.)
K_{h}	Gain in ROCOF control

Contents

List of Figures

List of Tables

1

Introduction

1.1 Background

The incorporation of Renewable Energy Sources (RES) such as wind power, solar Photovoltaic (PV), and Battery Energy Storage Systems (BESS) are rapidly increasing in power grids around the world [1]. This means that the percentage of total power that is provided by synchronous-based production decreases, while converter-based power generation increases which leads to new challenges in the power system. A key issue is that these RES do not contribute to system inertia as its default setting[2]. Taking wind power as an example, where the generator is connected to the grid via inverters that synchronously decouples the rotating mass of the generator from the grid [3]. Although this may not be a major concern in the Nordic synchronous area due to the large number of hydro plants, it could become problematic in other synchronous areas with low systemic inertia. To address this, there will be a growing importance for ancillary services, which typically include fast frequency reserve, reserves for frequency containment, frequency restoration, synthetic inertia and voltage regulation [4].

A potential solution is to provide synthetic inertia which can be implemented either through Grid Forming (GFM) or Grid Following (GFL) inverters. The GFM control strategy enables inverter-based energy sources to mimic the dynamic behavior of synchronous machines [5]. This type of inverter can regulate the grid voltage and frequency, meaning that it can operate in island-mode without any preexisting grid and provide ancillary services such as frequency containment reserve. On the other hand, the GFL control strategy requires an existing grid to synchronize its voltage and frequency output, which means that it cannot operate in island-mode without the presence of other GFM generators [6]. Although this simplifies the control algorithm compared to the GFM, it also limits its usage.

This thesis will be carried out during the winter and spring of 2025 at Solvina AB, a Swedish energy consulting company located in Mölndal. As many customers have similar systems, Solvina will through this project gain a better understanding of whether synthetic inertia is a feasible solution in weak grids, regarding frequency stability. In addition to having access to the model itself.

1.2 Aim

This master's thesis aims to evaluate the performance of GFM and GFL inverters' synthetic inertia and FFR capabilities in electrically weak grids. This will be achieved by developing a simulation model that can replicate grid frequency disturbances. The goal is to determine the effectiveness and stability margins of the GFM and GFL with respect to the stability of the grid frequency.

1.3 Limitations

The focus of this thesis lies on modeling control loops for GFM and GFL inverters connected to a RES, which are used to provide synthetic inertia to mitigate frequency disturbances. The system components will not be modeled in extensive detail, such as transformers or transmission lines. Instead, standard Simulink blocks will be used, as they are sufficient for the purpose of the simulations.

In Matlab and Simulink, an Electromagnetic Transient (EMT) model will be investigated. However, in most cases, the values of the Root Mean Square (RMS) will be taken into account to simplify the work [7]. The RMS analysis, although not as accurate as an EMT analysis, will provide acceptable accuracy and faster simulations.

Since the thesis is limited to disturbances in the grid frequency, such as frequency dips and phase angle jumps, there will be no voltage stability analysis carried out. The current provided from the RES to restore the frequency will therefore only be used to provide active power. Reactive power compensation will not be provided. Additionally, we assume that the RES has enough energy available to meet the demands of the synthetic inertia implementation.

Finally, the thesis work will not include any Frequency Restoration Reserve (FRR) to mitigate the steady-state error between the actual and the system frequency. This is assumed to be taken care of and is beyond the scope of consideration.

1.4 Specification of the issue being investigated

This thesis aims to investigate both technical and operational aspects of different control strategies for voltage source inverters, specifically with the goal of supporting grid frequency. The purpose of this thesis is also to consider the social, ethical, and ecological dimensions of these areas. The objective is to build and implement an inverter model in Simulink to explore the effectiveness of the synthetic inertia and Fast Frequency Response (FFR) produced, mainly in weak and island grids.

Initially, the concept of synthetic inertia and how it can be implemented in inverters connected to an external grid or operating in an island mode will be examined. An important distinction based on the literature between inertia, synthetic inertia, and FFR will be made to recognize the factors that differ between each concept. In this context, FFR is defined as the injection of active power proportional to the frequency deviation, and not as Fast Frequency Response as defined by Svenska Kraftnät.

The thesis will describe the implementation of an external grid with variable strength and an island grid constituted by a hydro power plant and a resistive load in the simulation environment. The implementation of inverter controllers will also be demonstrated, including mathematical descriptions of the parameters within the system. The different methods used to measure the frequency and filter signals in the simulation will be highlighted.

An evaluation of different GFL and GFM control strategies will be carried out. Based on the synthetic inertial response, Rate of Change of Frequency (RoCoF), and frequency nadir, the models will be evaluated to determine which is most suitable for specific cases. The different control strategies will also be pushed to find where they can no longer maintain stability. This will be achieved by a combination of increasing proportional gain, based on either RoCoF or a frequency deviation, and increased filtering. The goal is to use these findings to optimize inverter control schemes to help minimize frequency disturbances.

Additionally, the thesis will consider aspects other than the technical ones mentioned above. It will consider how synthetic inertia could affect the reliability of power systems in regions with low inertia and how it might change the public perception of reliability in the power system. The work will also include an examination of the environmental impact that increased synthetic inertia in power systems worldwide might have, such as an excessive need for mineral extraction.

2

Theory

This chapter presents the fundamental concepts and theoretical background relevant to the study. It begins with an overview of inertia in power systems, followed by different frequency estimations used today, operation and background of GFM and GFL inverters and passive filtering.

2.1 Inertia in Power Systems

The general term of inertia refers to the tendency of an object in motion to remain in motion for a short while after losing its propulsion. For instance, a car does not stop immediately as the gas pedal is released. In power systems, rotational inertia can be found in traditional power plants with rotating components, such as turbine rotors and flywheels.

Synchronous areas typically consist of several generators that rotate at different Revolution Per Minute (RPM) depending on the number of pole pairs, which typically results in a grid frequency of either 50/60 Hz depending on the region. During normal operation, the supply of active power and the load demand are of equal size, which results in a stable frequency in the grid. However, during a disturbance, such as the tripping of a generator or loss of a load, the difference between load and production is introduced, causing the frequency to deviate from its nominal value. Governors, the control system that regulates the mechanical input, responds to frequency changes by increasing or decreasing the active power. However, this adjustment takes time to apply due to several delays in the process. For instance, in a water turbine, there are delays such as the governor time constant itself and delays that are dependent on how quickly the water flow in the turbine's penstock can respond to changes in the guide vane position. Therefore, during frequency disturbances, inertia plays an important role in maintaining the frequency momentarily at its rated value while allowing enough time for the generating units to adjust to the change [8].

The difference in frequency due to the imbalance between load and generation is mathematically governed by the swing equation (2.1) [9].

$$2H\frac{d\omega}{dt} = T_m - T_e \tag{2.1}$$

Where H is the inertia constant in seconds, ω is the frequency in rad/s, t is the time in seconds, T_m is the mechanical torque from a turbine in one direction and

T_e is the electrical torque from a generator, opposite direction of T_m. From (2.1), it can be seen that if the mechanical and electrical torque are equal, there can be no acceleration or deceleration of the rotor, the frequency must be constant. This relationship is important because it describes how well a generator is working in sync with the grid. However, it is often easier to interpret the meaning of this equation in relation to active power instead of torque. To express the equation in active power, the following relationship is used:

$$P = T \cdot \omega \tag{2.2}$$

Assuming that the rotor speed ω is approximately constant and close to synchronous speed, in p.u. equal to one. Then the swing equation can be rewritten as:

$$2H\frac{d\omega}{dt} = P_m - P_e \tag{2.3}$$

Acceleration of the frequency is now represented by a change in the balance between the mechanical power input and the electrical power output to a Synchronous Generator (SG). From (2.3), the name swing equation becomes clear; the rotor angle of a machine accelerates, or *swings*, during a disturbance [9].

Changes in mechanical power input or electrical power output from a synchronous generator can occur for various reasons and are often difficult to predict. However, grid frequency instability is primarily caused by sudden changes in load demand or the disconnection of generation units, which lead to an imbalance in active power as described in (2.3).

From (2.3), the role of inertia in power system stability becomes very clear. As the inertia constant increases, the rotor angle accelerations decrease, resulting in smaller grid frequency deviations. The inertia of an entire synchronous area can be represented by the total system inertia constant.

$$H_{sys} = \frac{\sum Kinetic\ energy}{\sum S_{rated}} \tag{2.4}$$

Where S_{rated} is the base power of the system in MVA. The constant H_{sys}, represents the total kinetic energy stored in all rotating objects, in p.u. of the rated capacity. In other words, it indicates for how long generators can produce power at their rated capacity using only the stored rotational kinetic energy [10]. Typical values for the inertia constant in different production sources, as reported by ENTSO-E [11], are presented in Table 2.1.

Table 2.1: Typical inertia constants for different production types.

Production type	**Mean H(s)**
Nuclear	5.9
Fossil	4.2-4.3
Hydro	3.5-3.7
Biomass	3.3
Wind (onshore/offshore)	0
Solar	0

It can be observed that synchronous-based production units have relatively large inertia constants, reflecting their large rotating masses. In contrast, Inverter-based Resources (IBRs) such as wind and solar energy have inertia constants of zero.

2.2 Synthetic Inertia & FFR

As seen in the previous section, synchronous-based production units rely on the kinetic energy stored in rotating masses to provide an inertial response. IBRs, on the other hand, need to implement other strategies to mimic this behavior, which has been named synthetic inertia or FFR.

The term "synthetic inertia" has not been consistently defined within the industry. Initially, it was used to describe the rapid power injection from IBRs in response to grid disturbances [8]. However, many Transmission System Operators (TSO), such as SVK and Fingrid, now use the term FFR to describe ancillary services designed for rapid power injection during quick frequency deviations [12].

In contrast, this thesis uses the definition introduced by Robert Eriksson in [13], where the definition and distinction between FFR and synthetic inertia were coined. According to his definition, FFR refers to the controlled contribution of electrical torque from a unit based on frequency deviation. While the definition of synthetic inertia is defined as the controlled contribution of electrical torque from a unit that is proportional to the RoCoF. To clarify, this definition is not used by SVK but will be used in this thesis and can be summarized as:

$$FFR : P_{inj} \propto -\Delta f \qquad\qquad Synthetic\ inertia : P_{inj} \propto -\frac{d\Delta f}{dt}$$

Note that Δf is the frequency error ($f_{ref} - f_{actual}$) and not the time derivative.

2.3 Frequency & RoCoF

As explained in previous sections, when deviations occur between generation and load demand, there will be a deviation in frequency from the nominal value. The

RoCoF is the time derivative of the frequency deviation, and it is an important measurement of power system stability, which can be derived from the swing equation. From a frequency perspective, it is an indicator of the system's state of health [11].

$$RoCoF = \frac{d\Delta f}{dt} = \frac{\Delta P_m - \Delta P_e}{2H} \tag{2.5}$$

where Δf is the frequency deviation, P_m is the mechanical power, P_e is the electrical power, and H is the inertia constant. Equation (2.5 shows that a large RoCoF indicates a large power disturbance or a low inertia constant in the system.

According to the Swedish TSO Svenska Kraftnät (SVK), RoCoF during frequency events in the Nordic synchronous area is normally low. As an example, in events of large production losses, it can reach values of $0.1 - 0.2$ Hz/s, on rare occasions it may reach 0.3 Hz/s, and it would then be considered an extreme event. During these events, it is of great importance to keep power production running as further loss of production would increase RoCoF and could lead to the disconnection of units [14].

In other synchronous areas, where the penetration of inverter-based energy is greater, RoCoF values can be significantly higher. This causes problems as generating units are often equipped with RoCoF-based protection. For example, many wind farms are equipped with $2Hz/s$ RoCoF protection and would disconnect if this value is ever reached [15].

Many protection schemes that are used to regulate grid frequency rely on RoCoF to detect disturbances in the system. Since RoCoF is the time derivative of the frequency, this imposes strict requirements on the accuracy of the frequency measurements. However, RoCoF measurement includes an important trade-off between accuracy and the length of the measurement. For example, if a longer time period is utilized to measure RoCoF, it decreases the risk of false detection of frequency events. If a rapid response is necessary, the measurement window time period might have to be decreased, sacrificing some stability margins [16].

2.3.1 Frequency Estimation

It is important to have a robust and accurate estimate of the frequency in the grid to ensure complete system stability. Within the Nordic power system, consisting of Sweden, Norway, Finland, and Denmark, the normal frequency band is within 50 Hz ± 0.1 Hz. The frequency is allowed to deviate up to ± 0.5 Hz for a maximum of 5 minutes or ± 0.25 Hz for up to 15 minutes. After this time period, if the frequency does not settle, the system goes into *alert* state. In case of severe disturbances, the frequency is allowed to deviate up to ± 1 Hz for a maximum of 60 seconds. If the frequency does not settle, the system goes into the *emergency* state. In this state, load shedding may occur to prevent total system shutdown [17]. With this in mind, the importance of precise frequency measurement is evident. There are different methods used to estimate grid frequency; the following chapters will further explain the functionality and their advantages and disadvantages.

2.3.1.1 Zero Crossing Detection

The traditional and one of the most common approaches to measuring frequency is Zero Crossing Detection (ZCD) [18]. This method measures three-phase grid voltage or current and clocks the time between zero crossings. Since frequency is defined as the inverse of one time cycle, it is relatively easy and does not require much computational power to determine the frequency using this method. However, ZCD has proven not to be as reliable as other methods during faults in which phase angle jumps occur, or the voltage waveform is heavily distorted [19]. Cases have been recorded where, during faults, phase angle jumps have altered the time between zero crossings up to ± 33 % [20]. The ZCD method also requires significant filtering.

2.3.1.2 Phasor Measurement Unit

Another widely used measuring method is by using phasor measurement units (PMU). As the name indicates, a PMU is capable of measuring a voltage and/or current phasor consisting of a magnitude and phase angle. Based on phasor information, it can also provide operators with frequency and RoCoF estimations. PMUs can be synchronized via universal time-stamping and the use of a Global Positioning System (GPS). In the Nordic grid, PMUs are used in multiple substations as part of a Wide Area Monitoring System (WAMS). Nordic TSOs have committed to a goal in which WAMS is implemented throughout the entire grid by 2027 [21]. Since electric power grids are often spread across large geographical areas, it makes PMU:s the first choice of many TSO:s to monitor the grid. Problems related to PMU:s often relate to differences between manufacturers, such as different filtering methods [19]. Depending on the measuring algorithm, different units may produce variable results.

2.3.1.3 Phase Locked Loop

To estimate the grid frequency without relying on excessive filtering, which can distort the phase angle due to delays, Phase Locked Loops (PLL) are commonly used. The PLL itself introduces an internal delay due to its control structure, which means it can also act as a low-pass filter. As the name indicates, it functions by locking onto the phase angle of a sinusoidal three phase signal; how this is achieved is further explained in chapter 2.6. Since the frequency is the derivative of the phase angle, it becomes easy to estimate and is not as sensitive to disturbances as other methods, provided that the grid is strong enough. PLLs are advantageous to use for frequency estimation, as they are very fast and easily implemented without requiring a lot of computational power [22]. However, studies have found that PLLs may contain a steady state error unless they are tuned properly [23].

It is also important to clarify that while it is often stated that PLLs perform poorly in weak grids, the issue does not stem from the PLL itself. But instead, the problem arises when the voltage waveform that the PLL is measuring, becomes affected by active power injection, creating an unstable feedback loop. In the results section, this will be demonstrated.

2.3.1.4 Positive Sequence Phasor

Recent studies and reports have presented a frequency estimation method named Positive Sequence Phasor (PSP). The method is based on extracting the PSP of a three-phase sinusoidal signal, which can be a grid voltage or current. The PSP contains the fundamental component of the frequency harmonics, which makes it important for accurate frequency measurement. The three-phase signal is transformed into the $\alpha\beta$ frame using the Clarke transformation, and the PSP is then extracted using the symmetrical component transformation. Once the phase of the three-phase signal is extracted, the frequency can be estimated by its derivative over time.

According to [19], the PSP method provides a simple and robust frequency estimation which is suitable for power systems with high penetration of IBR. In [19], the PSP method was simulated using real-world frequency events and compared it with conventional frequency estimation methods. The results showed that the PSP method provided far superior frequency estimations during faults compared to ZCD, PMU, or PLL. However, this method has not been tested in real-world applications, as could be found in the available literature.

2.3.2 RoCoF Estimation

There are also various methods to implement RoCoF estimations. When using a PLL or zero-crossing detection, a commonly used implementation is to use the finite difference method (FDM), described in Figure 2.1 and (2.6).

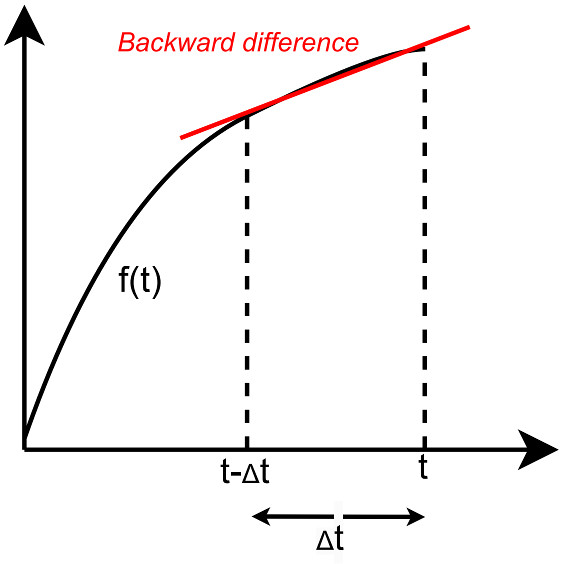

Figure 2.1: Backward difference (FDM).

$$RoCoF = \frac{f(t) - f(t - \Delta t)}{\Delta t} \tag{2.6}$$

This approach, used later in the simulations, estimates the derivative by taking the frequency measurement $f(t)$ at time t, comparing it with the previous measurement $f(t-\Delta t)$, and dividing the difference by the time interval Δt. Although this method is straightforward to implement in Simulink, it presents challenges, especially in low-inertia systems.

The FDM method relies on the assumption that the measured frequency between several time steps are relatively smooth. However, this is not the case in both reality and simulation, primarily due to the rapid change in frequency and the presence of noise in the system. As a result, two consecutive measurements could therefore differ significantly and lead to unstable or spiky RoCoF measurements. Furthermore, this method is highly sensitive to sudden phase angle jumps. To mitigate this, the use of low-pass filters or moving average filters is needed to smooth the data.

2.4 Grid Following Inverter

As indicated by the name, a key component in IBRs is the use of an inverter between the source and the grid. The purpose of the inverter is simply to convert DC power from the source or storage system to AC power, which can be used in the transmission network. What separates one inverter from another is mainly the control strategy or its mode of operation. A commonly used inverter in today's transmission systems is the GFL inverter [24][25], with its control strategy shown in Figure 2.2.

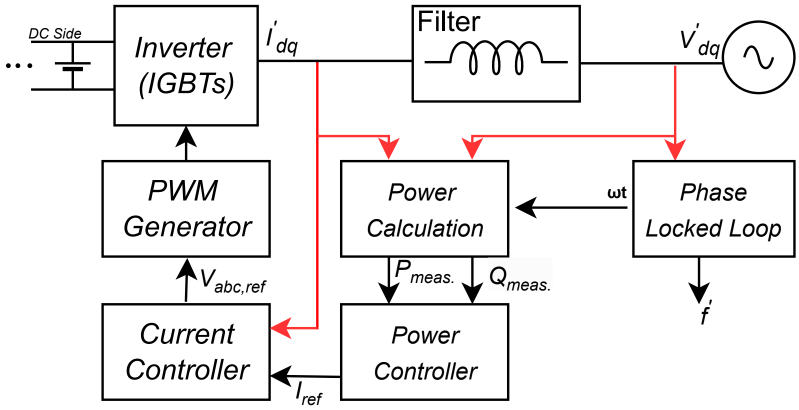

Figure 2.2: General model of a GFL inverter.

The GFL inverter operates similarly to a current source. It is not capable of generating its voltage or frequency at its Point of Common Coupling (PCC), but rather measures the voltage on the grid and synchronizes with its frequency. This is commonly achieved with the use of a PLL, which can extract both the frequency and the phase angle of the grid [26]. When locked to the frequency of the grid, it can adjust its active and reactive current according to the requirements of the grid.

As mentioned in the limitation section, this thesis focuses on frequency stability. Therefore, only active power injection is considered, making it redundant to include a reactive power reference value. However, the active power reference has to be calculated based on the grid frequency. The block diagram can be seen in 2.3.

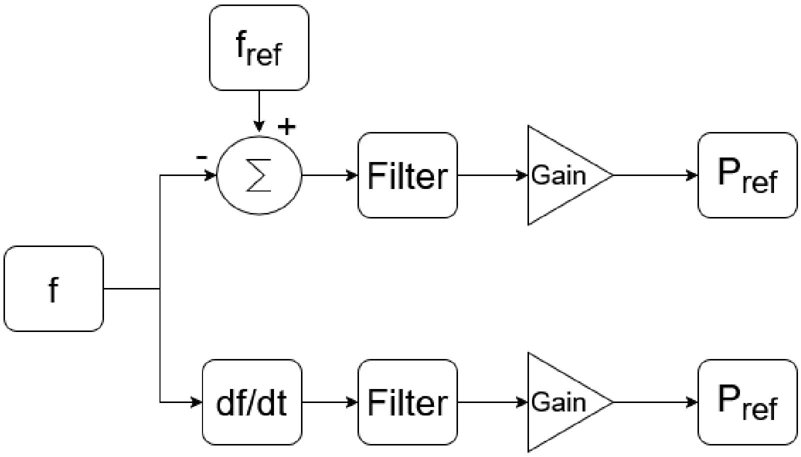

Figure 2.3: Power controller reference.

The power controller reference calculation is where the GFL inverter operation is decided. If it is calculated based on the frequency deviation the inverter is operating in FFR mode. If it is calculated based on the frequency derivative then the inverter is operating in synthetic inertia mode. The filter block is used to attenuate high frequency noise. The gain block is used to calculate the active power reference, based on the relationship described in section 2.2

The second component of the power controller is a PI regulator, which generates its output signal for the current controller, as illustrated in Figures 2.4a and 2.4b, respectively.

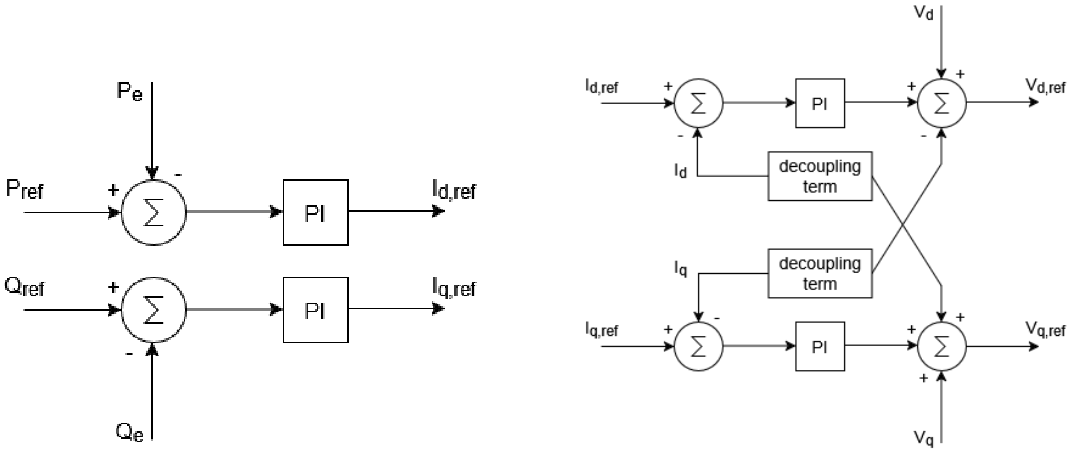

(a) General model of a power control loop

(b) General model of a current control loop

Figure 2.4: Power and current control loops.

The power control loop measures the active and reactive power output of the inverter and compares it to their respective reference values. A proportional-integral (PI) regulator is then used to adjust the power injection. The resulting power control output serves as the reference for the current control loop, which also employs a PI regulator to regulate the active and reactive current components. The output of the current control loop becomes voltage reference, which is used to generate the PWM signals for the inverter [27].

2.5 Grid Forming Inverter

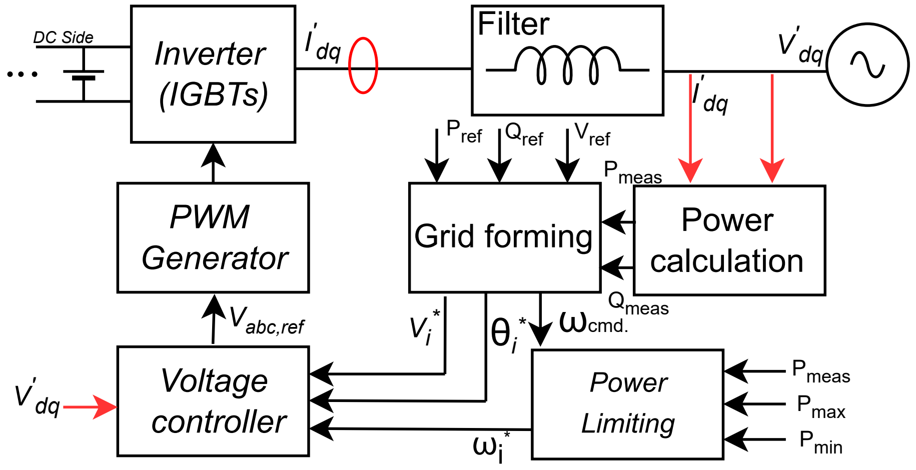

Figure 2.5: General model of a GFM inverter.

Another type of inverter is the GFM inverter, which has emerged as a potential solution to the growing stability challenges caused by the lack of voltage and frequency regulating units. Although GFM technology began to appear as early as the year 1990, mainly to operate in island-mode, it was not until 2015 that GFM technology took off and gained a lot of attention [28].

While GFL inverters measure the voltage at the PCC for synchronization purposes, the primary objective of the GFM inverter is rather to form the PCC voltage and frequency. This means that a GFM inverter operates as a controllable voltage source, similar to synchronous generators, constantly “ready” to support the grid. The use of GFM inverters can be advantageous from a frequency stability point of view. Due to the fact that it continuously maintains the grid conditions, the GFM inverter can respond effectively to disturbances with minimal delay, enabling a significantly faster response in terms of power injection compared to GFL inverters [5].

GFM technology is an evolving area due to the rapid increase of RESs in power systems. Many different control strategies have emerged as a result of this, all of them with their strengths and weaknesses. The main objective of the control system is often to provide inherent inertia, or synthetic inertia, similar to SGs [28]. According to [5], control strategies can be divided into *droop-based control*, *synchronous machine-based control*, or *other types of control*, where every group has several subgroups. Some of the available control strategies are listed below.

2.5.1 Frequency-Based Droop

Droop-based control is the oldest and most tested, and it is adopted from the control strategy that allows for several SGs to operate in parallel. This type of controller enables GFM inverters to operate not only in smaller island grids but also in large-scale power grids. Droop-based control can be further categorized into groups such as frequency-based, angle-based, or Power Synchronization Control (PSC). In Figure 2.6, frequency-based droop control is presented.

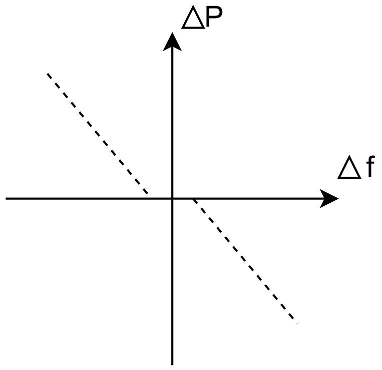

Figure 2.6: Frequency-based droop control strategy.

When GFM control strategies emerged during the 1990s, droop-based control was the preferred method. In this control strategy, a linear relationship between frequency error and active power deviation is defined using a droop coefficient. This relationship could also be reactive power against voltage, etc. As the frequency of the grid fluctuates, the inverter regulates its active power output to mitigate disturbances. The droop coefficient, K_{droop}, is the amount of active power injected into the grid when it is subjected to a frequency disturbance and is calculated according to (2.7). Frequency-based droop is common among GFM control strategies, while other methods, such as the virtual synchronous machine (VSM), utilize a droop-based active power error to calculate the output frequency.

$$K_{droop} = \frac{\Delta P}{\Delta f} \tag{2.7}$$

Where Δf is the frequency deviation in p.u. from f_0 and ΔP is the active power injection in p.u. as a response to the frequency deviation. This control strategy is very simple as it is based solely on local measurements [25]. As mentioned in section 2.2, this control strategy is used to provide FFR as active power injection is proportional to the frequency deviation, according to [13].

2.5.2 RoCoF-Based Synthetic Inertia

Compared to the frequency-based droop control, which is used to improve steady-state frequency deviations, the RoCoF-based controller is used to mitigate large frequency derivatives and improve the frequency nadir. This control strategy implements synthetic inertia according to sections 2.2 and [13] by injecting an amount of active power which is proportional to the RoCoF, as seen in (2.8).

$$K = -\frac{\Delta P}{\frac{df}{dt}} \tag{2.8}$$

The main issue when implementing RoCoF-based droop is the accuracy of the measurement, as mentioned in section 2.3.2. It is important to have robust and sophisticated filtering when measuring RoCoF as it might introduce faulty estimations otherwise. Figure 2.3, showed the power controller where filters (either low-pass or moving average) are applied to minimize the high-frequency components from the frequency and frequency derivative measurements. Studies in which low-pass filtering has been applied to RoCoF measurements have shown that adjusting the filter cutoff frequency may greatly improve the level of synthetic inertia, resulting in better RoCoF and frequency nadir [29]. Similarly, the droop coefficient, K_{droop}, should be tuned along with the cutoff frequency to find an optimal solution to determine how much active power can be injected compared to how much filtering is necessary.

2.5.3 Virtual Synchronous Machine

As has previously been mentioned, due to the increase in IBRs in the grid, it has become attractive for inverter control systems to emulate the behavior of SGs. Especially for the purpose of grid frequency stability [30]. The VSM control strategy allows IBRs to operate similarly to an SG. VSM aims to provide the grid with inertial power when it is subjected to disturbances. This is achieved through a control structure that utilizes the speed dynamics of an SG (i.e., the swing equation, shown in Figure 2.7) and, in many cases, also a frequency-based droop characteristic [31].

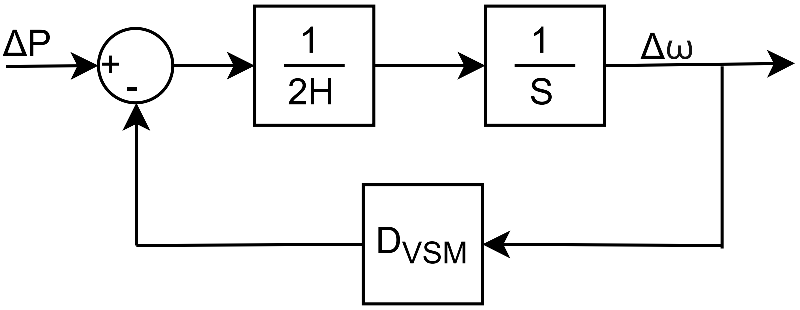

Figure 2.7: Block diagram of the VSM swing equation.

Using software, the SG speed dynamics can be emulated so that both the inertial power from the stored energy in the rotating mass and the damping provided by friction and damper windings are included in the inverter control.

2.6 Phase Locked Loop

A PLL is a closed-loop control system that continuously monitors and adjusts its output based on feedback. It is commonly used in many fields such as power electronics (e.g., GFL inverters), telecommunications, computers, and radio frequency applications. The primary function of a PLL is to synchronize its internal oscillator with an external signal in terms of phase and frequency. Common applications for PLLs can therefore be to generate stable frequencies, recover signals with a low signal-to-noise ratio, and control clock pulses.

In GFL inverters, as mentioned in the previous chapter, the PLL plays a crucial role by ensuring that the inverter stays synchronized with the grid, since the GFL cannot generate its own frequency and voltage. This ensures that the inverter is injecting active power at the same frequency as the grid. The basic structure of a PLL consists mainly of three components: The phase detector, loop filter, and Voltage Controlled Oscillator (VCO).

The PLL synchronizes the output signal V' with the external signal V. The phasor detector block compares the phase difference between the input signal and the output signal and outputs a voltage proportional to the phase error ϵ_{pd}. The error is then sent to the second block, which is the loop filter, which consists of either a first-order low-pass filter or a PI controller. The objective of this block is to attenuate the high-frequency AC components that are produced from the phase detector. The third and last block is the VCO, which can be thought of as a voltage-to-frequency converter. This block generates an AC signal whose frequency is based on the output voltage of the loop filter V_{LF} [32].

Additional techniques or modifications can be applied to the PLL depending on its usage and application, and the model described above represents only a basic version of the actual device. In addition, while the loop filter attenuates the high-frequency components of the input signal, the VCO contributes to the unwanted noise itself, which is called *phase noise*, which is not filtered out. However, this is more significant at higher frequencies and therefore can be neglected for grid frequencies [22].

2.6.1 The Synchronous Reference Frame PLL

The Synchronous Reference Frame PLL (SRF-PLL) is a commonly used PLL for grid synchronization in three-phase systems. Due to its frequency insensitivity, meaning its ability to accurately track the phase and amplitude of the grid voltage during frequency events, it is suitable for this application [32]. The SRF-PLL converts the three-phase voltage vector from the ABC frame to the dq rotating reference frame using Park's transformation, shown in (2.9).

$$\begin{bmatrix} d \\ q \\ 0 \end{bmatrix} = \frac{2}{3} \begin{bmatrix} \sin(\theta) & \sin\left(\theta - \frac{2\pi}{3}\right) & \sin\left(\theta + \frac{2\pi}{3}\right) \\ \cos(\theta) & \cos\left(\theta - \frac{2\pi}{3}\right) & \cos\left(\theta + \frac{2\pi}{3}\right) \\ \frac{1}{2} & \frac{1}{2} & \frac{1}{2} \end{bmatrix} \begin{bmatrix} a \\ b \\ c \end{bmatrix} \tag{2.9}$$

This transformation produces three components: The *d*-component that represents the voltage aligned with the rotating reference frame, the *q*-component that represents the voltage orthogonal to the reference frame, and the zero sequence component that represents any imbalance between the three phases. Although the zero-sequence component can be significant during a grid fault or unbalanced condition, the simulations will assume a balanced grid, and it can therefore be neglected.

In the synchronous reference frame, the components of the d- and q-axis are decoupled, often in such a way that they can regulate active and reactive power separately. The SRF-PLL can be designed to regulate the output of the d-component or the q-component, depending on the application. In this case, setting the q-component to zero is the normal operation mode, as shown in Figure 2.8, since injecting active power is the main objective. In other applications where injecting reactive power is the primary goal, such as the STATCOM, it is more common to set the d-component to zero [33]. By setting the q-component to zero, the PI controller will adjust its estimated phase angle θ so that, in a steady state, the reference frame will be perfectly aligned with the grid voltage.

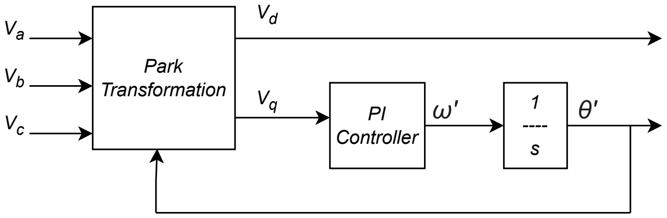

Figure 2.8: Block diagram of the SRF-PLL.

3

Simulink model design and implementation

This chapter provides a detailed description of the implementation of the MATLAB/Simulink system for both the island operation and the strong grid. It will cover the design process and the selection of system parameters. Given the similarities between the two systems, the first section will go through the shared implementations in both grids. In the latter sections, the focus will shift to the specific differences within each system. It should be noted that the implemented model is fundamentally an EMT model, representing waveforms in individual phases. However, in this thesis, it is primary used and analyzed as an RMS model as focus lies on the fundamental frequency behavior rather than EMT phenomena.

3.1 Shared system parameters

In this section, all shared system parameters are described. These include the inverter models, step-up transformer and the transmission line. The block diagram is shown in Figure 3.1.

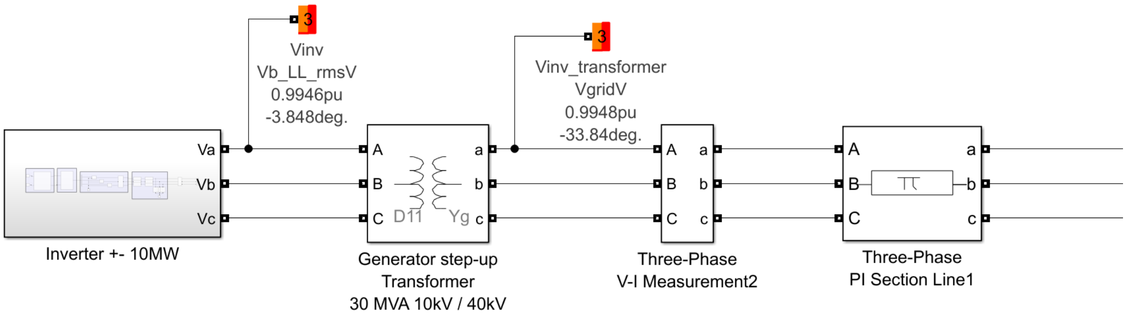

Figure 3.1: Shared system components.

3.1.1 Declaration of p.u. base quantities

In order to reduce computational load and simplify the evaluation of the system's performance, the controllers will be defined in per unit (p.u.). In short, the per unit system normalizes the variables by expressing them as a fraction of a chosen base value. This will also ensure that the PI controllers remain properly tuned regardless of the power levels in the system as they are instead tuned for the normalized interval.

The base quantities for voltage, current, power, and impedance were selected according to standard practices for power systems, as described in Prabha Kundur's "Power System Stability and Control" [9]. However, the base power and line-to-line voltage were chosen to mimic a typical regional network.

$$V_b = Z_b I_b = \frac{V_{b,LL,rms}}{\sqrt{3}}\sqrt{2} \quad \text{base voltage, phase peak} \tag{3.1}$$

$$I_b = \frac{S_b}{V_b \cdot 3/2} \quad \text{base current, phase peak} \tag{3.2}$$

$$\tag{3.3}$$

$$Z_b = \frac{V^2_{b,LL,rms}}{S_b} = \omega_b L_b \quad \Omega\text{, base impedance} \tag{3.4}$$

$$\omega_b = 2\pi f_n \quad \text{rad/s, angular frequency} \tag{3.5}$$

$$L_b = Z_b/\omega_b \quad \mu\text{H, base inductance} \tag{3.6}$$

Variable	**Value**
S_b	10 MVA
S_{gen}	40 MVA
$V_{b,LL,rms}$	400 V
V_b	326.59 V
V_{grid}	40 kV
I_b	20.41 kA
Z_b	0.016 Ω
ω_b	314.16 rad/s
L_b	50.93 μH
f_n	50 Hz
f_{sw}	5 kHz

Table 3.1: Base values used in the system.

3.1.2 Voltage Source Inverter

The theoretical model of the GFL and GFM inverters includes a pulse width modulation (PWM) generator and insulated gate bipolar transistor (IGBT) switches between the current controller and the output of the inverter. However, as stated in the limitations chapter, although the model uses an EMT representation with ideal switching, the analysis is based on RMS quantities, meaning that small-time-scale phenomena, such as PWM switching and its associated harmonics, are considered negligible. To simplify the model, a controlled voltage source block, shown in Figure 3.2, replaces the PWM generator and IGBT switches, reducing complexity and computational effort.

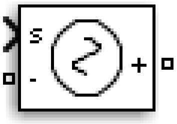

Figure 3.2: Controlled voltage source block.

Here, the positive and negative terminals of the block correspond to those of a voltage source, while the "S" terminal represents the input reference signal. In other words, the voltage source will take the input reference signal and output a physical voltage source signal.

3.1.3 Filter

Due to the usage of the controlled voltage source, the harmonics that the real filters would attenuate are more or less negligible in the simulation. Therefore, the filter will not serve the purpose of harmonic attenuation but instead remain in the system to ensure that the current controller operates as it would with a filter present.
The filter inductance and capacitance were designed as a typical value of 0.1 p.u. The filter X/R ratio was chosen as 1/100, resulting therefore in a filter resistance of 0.001 p.u., in Figure 3.3, the Simulink block diagram is shown.

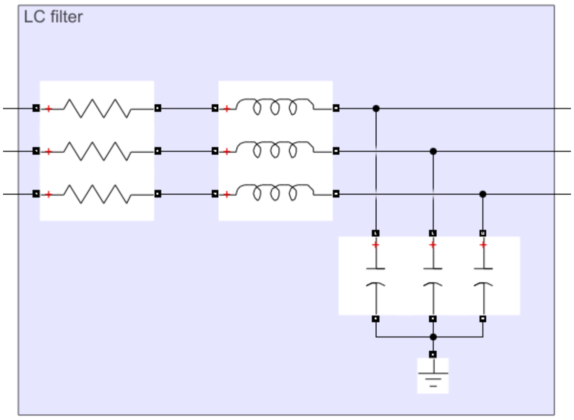

Figure 3.3: RLC filter used in the inverter

3.1.4 Step response assessment

The controllers in the upcoming sections will follow a first-order response, described by the following equation:

$$y(t) = K \cdot u(t)(1 - e^{-t/\tau})$$

where K is the gain, $u(t)$ is the input, t is the time, τ is the time constant, and $y(t)$ is the output. Setting $t = \tau$, the formula simplifies as $e^{-\tau/\tau} = 0.368$:

$$y(\tau) = 0.632\ K \cdot u(\tau) \tag{3.7}$$

This shows that after one time constant τ, the output will have reached 63.2% of the final steady state value. This is a standard approach for determining the time constant of a first-order system and will be used to help determine the proportional and integral parameters.

The magnitude of the overshoot is denoted by the letter M and is expressed as a percentage of the steady state value according to the formula:

$$M = \frac{X_{peak} - X_{Steady\ state}}{X_{Steady\ state}} \cdot 100 \tag{3.8}$$

3.1.5 Current Controller

The objective of the current controller is to regulate the d- and q-axis currents of the inverter to follow their respective reference values i_{dref} and i_{qref}. It is included in the GFL inverter and ensures that the inverter will provide adequate active and reactive power to the grid. The Thevenin model can be described as shown in Figure 3.4. In both practical implementations and the simulations, the filter can be an LC filter which introduces a capacitance to the Thevenin model. However, for the current controller, simplification is possible, as the Thevenin equivalent of the grid is seen from the bus where the capacitor is connected to.

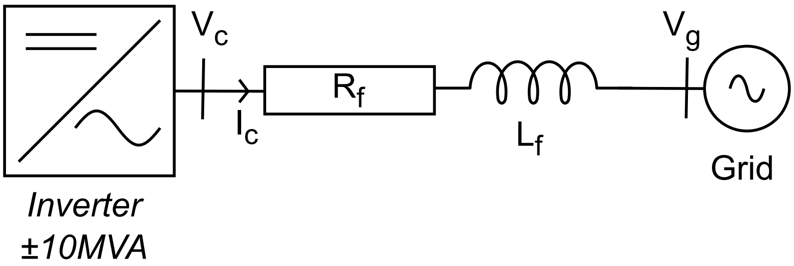

Figure 3.4: Thevenin grid model.

According to Kirchhoff's voltage law, the model can be expressed in the ABC-frame as

$$V_c = R_f \cdot i_c + L_f \cdot \frac{di_c}{dt} + V_g \tag{3.9}$$

Where V_c is the terminal voltage of the inverter, R_f and L_f are the resistance and inductance of the filter, and V_g is the voltage of the grid. The most common approach to model a current controller is to have it operate in the synchronous reference frame (dq-frame) in p.u. The strategy follows the approach presented in [34], which has been adapted for inverter control. After first transforming (3.9) into $\alpha\beta$, using the Clark transformation, and then into dq-coordinates using the Park transformation (2.9), (3.9) can be expressed as:

$$V_{c,dq} = R_f i_{c,dq} + j\omega L_f i_{c,dq} + L_f \frac{di_{c,dq}}{dt} + V_{g,dq} \tag{3.10}$$

To find the per-unit formulation of the equation, both the left-hand side and the right-hand side have to be divided by the base quantity V_b. To simplify calculations, (3.1), (3.4) and (3.6) were used to express V_b in terms of base impedance, inductance and angular frequency.

$$\frac{V_{c,dq}}{V_b} = \frac{R_f}{Z_b} \cdot \frac{i_{c,dq}}{I_b} + \frac{j\omega}{\omega_b} \cdot \frac{L_f}{L_b} \frac{i_{c,dq}}{I_b} + \frac{\frac{L_f}{L_b}}{\omega_b} \frac{di_{c,dq}}{dt} + \frac{V_{g,dq}}{V_b} \tag{3.11}$$

Simplifying this equation into p.u, where $\frac{\omega}{\omega_b}$ equals to one, yields

$$V_{c,dq}^{pu} = R_f^{pu} i_{c,dq}^{pu} + jL_f^{pu} i_{c,dq}^{pu} + L_f^{pu} \frac{di_{c,dq}^{pu}}{dt} + V_{g,dq}^{pu} \tag{3.12}$$

separating the equation into V_d^{pu} and V_q^{pu}.

$$V_d^{pu} = R_f^{pu} I_d^{pu} + jL_f^{pu} I_q^{pu} + L_f^{pu} \frac{dI_d^{pu}}{dt} + V_{g,d}^{pu} \tag{3.13}$$

$$V_q^{pu} = R_f^{pu} I_q^{pu} - jL_f^{pu} I_d^{pu} + L_f^{pu} \frac{dI_q^{pu}}{dt} + V_{g,q}^{pu} \tag{3.14}$$

Here, it can be seen that the terms $+L_f^{pu} I_q^{pu}$ in the d-axis equation and $-L_f^{pu} I_d^{pu}$ in the q-axis equation introduce coupling between the two axes. In this case, coupling refers to the unwanted interaction between the I_d and I_q currents where a change in either of them will influence the other, resulting in worse performance for the controller. Therefore, a cross-decoupling term needs to be introduced to compensate for this, making the current controller able to control each axis independently.

To build the current controller, the transfer function of the grid model has to be defined and will be designed to have a first-order response. From 3.12 in the Laplace domain, this becomes

$$G(s) = \frac{i_{c,dq}^{pu}(s)}{V_{c,dq}^{pu}(s) - V_{g,dq}^{pu}(s) - j\omega L_f^{pu} I_{c,dq}^{pu}(s)} = \frac{1}{\frac{L_f^{pu}}{\omega_b} s + R_f^{pu}} \tag{3.15}$$

and the closed-loop transfer function, where F(s) is the transfer function of the current controller, becomes

$$\frac{i_c^{pu}(s)}{i_c^{*pu}(s)} = \frac{F(s)G(s)}{F(s)G(s) + 1} = \frac{\alpha_{cc}}{s + \alpha_{cc}} \tag{3.16}$$

where * denotes the reference value, from (3.15) and (3.16), the output and input of the PI controller F(s) will then be

$$F(s) = \frac{V_{c,dq}^{pu}(s) - V_{g,dq}^{pu}(s) - j\omega L_f^{pu}}{i_{c,dq}^{*pu}(s) - i_{c,dq}^{pu}(s)} \tag{3.17}$$

and the current controller can then be designed as

$$V_{c,dq}^{*pu}(s) = (K_{P,cc} + \frac{K_{I,cc}}{s})(i_{c,dq}^{*pu}(s) - i_{c,dq}^{pu}(s)) + V_{g,dq}^{pu}(s) + jL_f^{pu} i_{c,dq}^{pu}(s) \tag{3.18}$$

In Figure 3.5, the implementation of (3.18) is shown as a block diagram. Measurements of voltage and current used as input to the current controller are denoted by "B1" or "B2" in the figure, depending on where the measurements come from in the grid model, this is to simplify the implementation work.

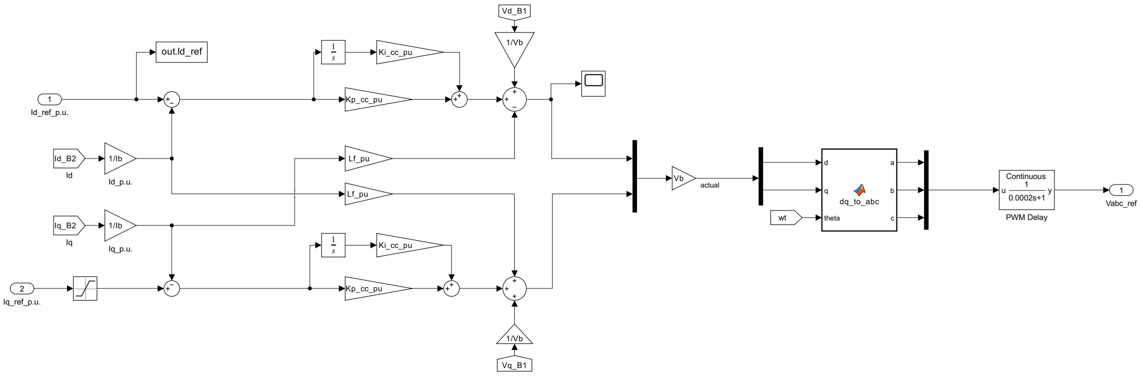

Figure 3.5: Block diagram of the Current Controller

It can also be observed that, in addition to the cross-decoupling term, two other inputs not previously mentioned in detail are the feedforward terms V_d and V_q. A feedforward regulator is a regulator that uses information from a measurable disturbance to improve the regulation. In this case, by measuring the voltage V_g, the controller will be able to act fast against any changes in the voltage of the grid. Thus, compensating for them directly without waiting for the PI controller to react to changes in the reference currents.

The PI controller parameters K_p and K_i were calculated using a bandwidth (α_{cc}) of $2\pi 100$ rad/s to ensure a fast response from the inner control loop. This will be the basis for calculating the bandwidth of the outer control loop.

$$F(s) = K_{P,cc} + \frac{K_{I,cc}}{s} = \frac{\alpha_{cc}}{G^{-1}(s)} = \frac{\alpha_{cc} L_f^{pu}}{\omega_b} + \frac{\alpha_{cc} R_f^{pu}}{s} \tag{3.19}$$

Using these values resulted in a time constant $\tau_{r,cc}$, of approximately 1.65 ms.

3.1.6 Power controller

In figure 3.6 the block diagram of the power controller implemented in Simulink is presented. It utilizes a PI controller to regulate its output according to the reference input. If the frequency in the grid is stable, there will be no active power injection from the GFL inverter. Therefore, the power reference is zero. However, during frequency disturbances the power reference will change depending on the mode of operation. The output of the controller is passed through a saturation block of ± 1 pu to ensure that the GFL inverter does not inject more active power than it is capable of. Normally, if active power is limited to 1 p.u. of the MVA rating, there will be no space for reactive power. However, in this case, unity power factor is assumed as Iq_{ref} is set to zero. Also, a simple anti-windup function was implemented to prevent integrator windup.

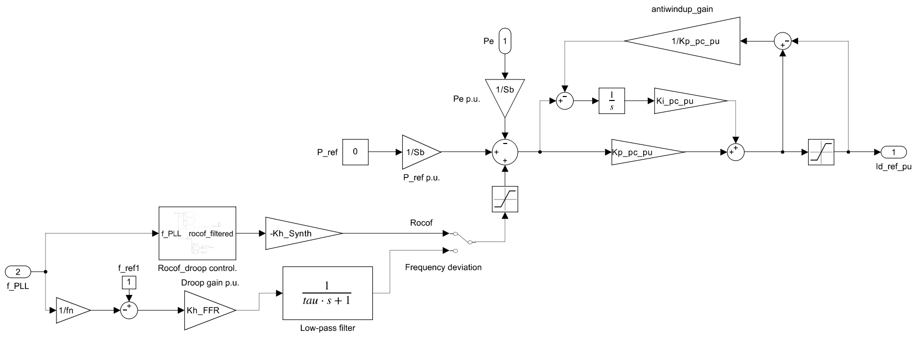

Figure 3.6: Block diagram of the Power Controller

The power controller is used to determine whether the GFL inverter is operating in FFR mode or in synthetic inertia mode. When operating in FFR mode, the active power reference is calculated according to (3.20).

$$K_{FFR} = \frac{\Delta P}{\Delta f} \tag{3.20}$$

In this equation ΔP is the active power reference in p.u., Δf is the frequency deviation in p.u. and K is the regulating strength. On the other hand, when the GFL inverter is operated in synthetic inertia mode, the active power reference is calculated according to (3.21).

$$K_{synth} = -\frac{\Delta P}{\frac{df}{dt}} \tag{3.21}$$

Here, ΔP is the active power reference in p.u., $\frac{df}{dt}$ is the RoCoF in Hz/s and K is the regulating strength in p.u./(Hz/s). Both signals, Δf and RoCoF, are passed through a filter with variable time constant.

The power controller in figure 3.6 is used to regulate $I_{d,ref}$ to the current controller. It is the outer control loop of the system, and the current controller is the inner control loop. Generally, it is desirable for the inner loop to be approximately ten times faster than the outer loop. This was achieved by generating a step response in the power controller and changing $K_{P,pc}$ and $K_{I,pc}$ until the time constant $\tau_{r,pc}$ was approximately equal to $10\tau_{r,cc}$.

3.1.7 PLL

The block diagram in Figure 3.7 illustrates the implemented PLL.

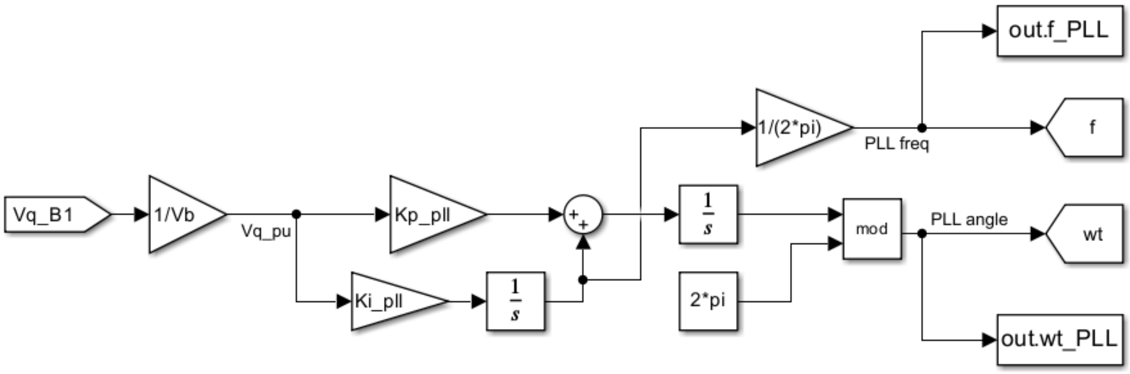

Figure 3.7: Block diagram of the PLL

The input $V_{q,b1}$ represents the voltage across the filter capacitor, which is first normalized by dividing by the base voltage Vb, resulting in the per unit value $V_{q,pu}$. This signal is then sent to the PI regulator, where the angular frequency is derived from the integral part only to avoid fluctuations from the proportional term. Dividing the angular frequency by $\frac{1}{2\pi}$ then yields the estimated frequency at the inverter. The phase angle is derived by integrating the summed angular frequency and, for simplification, it is wrapped between 0 and 2π, using a modulo block.

3.1.8 Transmission Line

The grid model was connected to the inverter model via a three-phase PI section transmission line at 40kV with variable length. The positive sequence values of R, L and C can be seen in table 3.2.

Variable	**Value**
R_1	0.01 Ω/km
L_1	1.02 mH/km
C_1	0.011 F/km

Table 3.2: Transmission line resistance, inductance & capacitance

3.1.9 Transformers

Three-phase transformers (two windings) transform 10 kV voltages from the inverter and the SG to the rated voltage of 40 kV. In the model, the step-up transformers were configured with no saturation and were parametrized as follows:

Variable	Value	Description
$S_{GSU,gen}$	20	MVA
$S_{GSU,inv}$	10	MVA
R_{GSU}	0.001	p.u. copper resistance
X_{GSU}	0.15	p.u. leakage reactance
$R_{m,GSU}$	500	p.u. core losses resistance
$X_{m,GSU}$	500	p.u. magnetizing reactance

Table 3.3: Base values used for the transformer.

3.1.10 Solver configuration

For the simulation of the system, the variable-step solver ”ode23tb” was used. This was selected because systems modeled using Simscape Electrical can include non-linear components such as power electronics which require a stiff solver [35]. ode23tb is, a solver that can solve differential equations in which some variables in the system may change rapidly, whereas other solvers can become unstable. The maximum step size was set to $1e^{-4}$ seconds, relative tolerance of $1e^{-3}$, and absolute tolerance set to auto.

3.2 Island grid

In this section, the system parameters and blocks specific to the island grid, shown in Figure 3.8 are described. The island grid consisted of a hydro power plant in parallel the inverter, connected to a load.

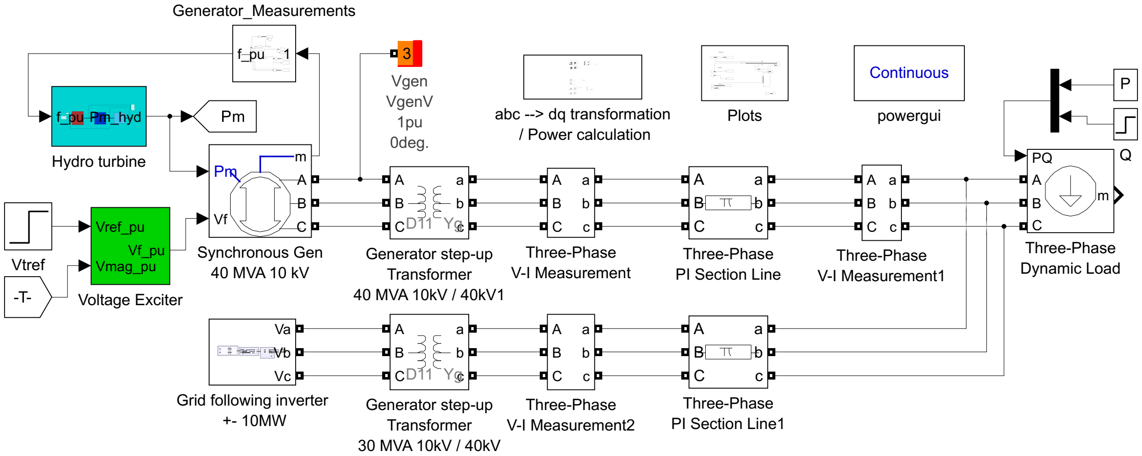

Figure 3.8: Block diagram of the island mode simulation.

3.2.1 Synchronous Generator

To simulate a realistic response in the island-mode operation case, a SG of 40 MVA and 10 kV, modeled as a swing generator, was used to represent a hydropower station. In other words, when performing the load flow analysis, the generator will act as both the reference point for the voltage magnitude and the phase angle. The inputs to the generator are the mechanical power P_m and the excitation voltage V_f. The generator was characterized with an inertia constant of 2.5 s, which is a typical value for a small to medium-scale hydro generator. The mechanical friction coefficient was set to 0 p.u., indicating that there were no damping losses. In summary, the generators were defined as follows:

Table 3.4: Synchronous generator parameters.

Parameter	**Value**
Nominal Power	40 MVA
Line-to-line voltage	10 kV
Inertia coefficient H(s)	2.5 s
Mechanical friction D_w	0 p.u.
Synchronous reactance X_d	2.6 p.u.
Transient reactance X'_d	0.28 p.u.
Subtransient reactance X''_d	0.21 p.u.
Stator resistance R_s	0.003 p.u.

The values provided in table 3.4, especially the reactances, are typical values for turbo generators, such as a gas turbine generator. However, reactances in a water turbine generator are typically smaller, making this a more severe operating condition, and thus an acceptable one.

3.2.2 Hydro turbine

The hydro turbine controls the mechanical power inputted to the generator and was modeled as three components: The governor, the gate actuator, and the penstock.

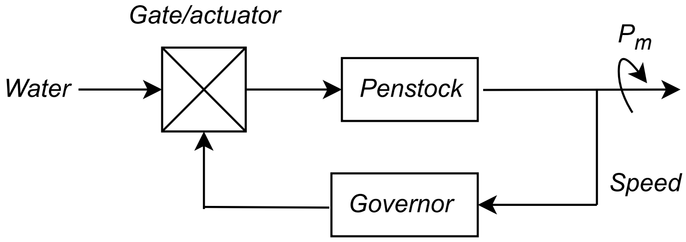

Figure 3.9: Block diagram of the turbine governor.

The gate actuator controls the flow of water into the turbine by adjusting the gate position based on a reference signal from the governor. In Simulink, this block represents the time delay of the servo motor, $T_{ser} = 0.2\ s/rad$, and the servo motor speed limit, $A_{ser} = 1\ pu$.

The penstock represents the waterway that leads to the turbine. When simulating a load step, the actuators will open/close the guide vanes depending on the desired output power. In the case of opening the vanes, there will be an initial pressure drop throughout the penstock due to the time it takes for the water to reach the turbine. This results in a delay/temporarily reduced output power in the turbine until the water pressure has had time to build up once again. In the Simulink model, the water time constant T_w was set to 0.5 s.

The generator frequency f_{pu} was derived from the rotor speed ω_m (from the generator measurement block) and fed to the governor to find the frequency error Δf. The controller was defined as follows:

$$G_{\text{ref}}(s) = \left(K_{p_G} + \frac{K_{i_G}}{s}\right) \cdot (\Delta f - (R_G \cdot (G_a - P_{m0})) \tag{3.22}$$

and in Figure 3.10 the corresponding block diagram is shown.

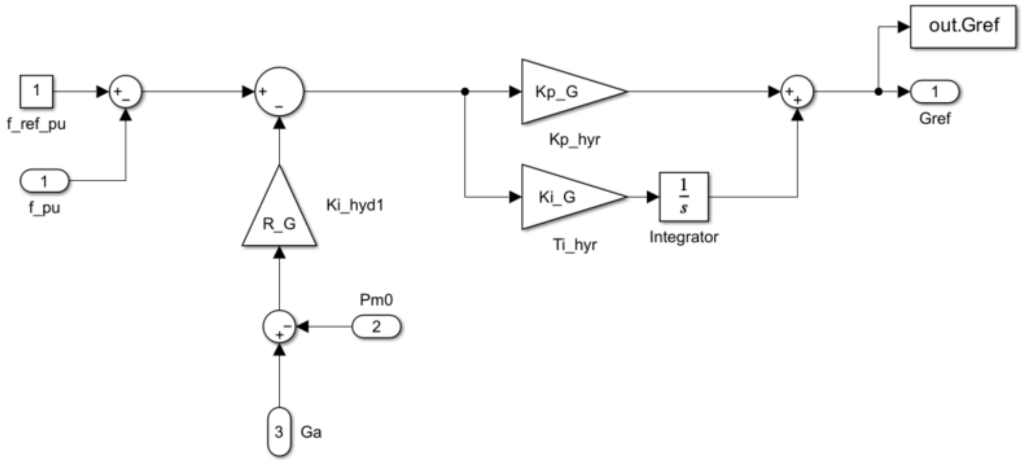

Figure 3.10: Hydroturbine regulator

The hydroelectric power station utilizes a droop-based speed governor with a constant of $R_g = 6\%$. P_{m0} is the initial steady state mechanical power and Ga is the output signal from the gate actuator. The proportional and integral gains $K_p = 5$ pu and $K_i = 1$ pu were selected based on the typical values used for similar hydropower stations.

3.2.3 Excitation system

While the primary focus of this thesis lies in frequency and active power control, the Automatic Voltage Regulator (AVR), or voltage exciter, is important to include for the SG. The AVR ensures that the generator's output voltage remains constant at variable loads by adjusting the excitation voltage. Similarly to turbine mechanics, the voltage exciter consists of delays, limiters, PI controllers, and sensor filters.

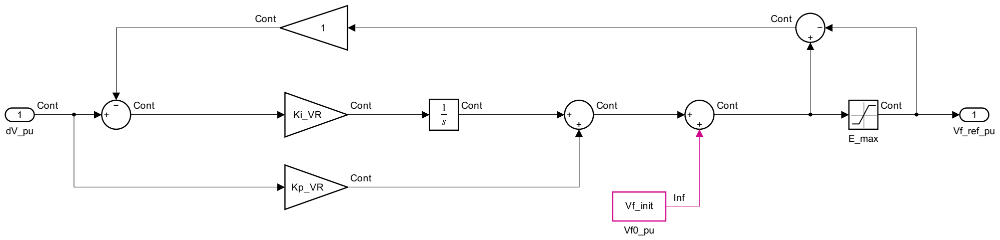

Figure 3.11: AVR block diagram.

3.2.4 Three-phase Dynamic Load

The Three-Phase Dynamic Load block models a load with active and reactive power consumption without any negative or zero-sequence currents. In the simulations, external control of PQ using step blocks was used to set the initial and final active power values at a specified step time.

3.3 External Grid Connected Model

This section presents the methodology used to model the inverter operation towards an external grid with variable strength.

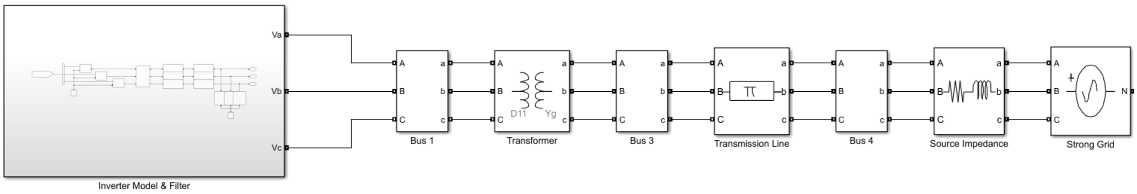

Figure 3.12: Variable Grid - GFL Simulink Model

The inverter model is connected to an external grid represented by a three-phase programmable voltage source block with a variable impedance connected in series. According to 3.4, if the impedance is infinitely small, it would correspond to an infinitely large base power. The programmable voltage source block can generate three-phase sinusoidal voltages with a predetermined frequency, initial phase angle, and amplitude. It is capable of introducing time-variable step or ramp signals of frequency, phase, or amplitude, making it suitable for analyzing the inverter operation when disturbances occur in the main grid [36]. However, by using this model it is not possible to analyze power or frequency oscillations, such that would occur between two generators. The voltage source is an ideal stiff source, therefore the stability analysis in these cases focuses on the stability of the GFL inverter control system.

3.3.1 Variable Grid Strength

To be able to change the grid model Short Circuit Capacity (SCC) and XR_{ratio} a three-phase series impedance consisting of resistance and inductance was connected to the programmable voltage source. The following method was used to calculate the source impedance based on predetermined SCC and XR_{ratio}.

$$Z_{src} = \frac{V_{LL,RMS}^2}{S_{sc}} \tag{3.23}$$

The source impedance should consist of resistance and reactance:

$$Z_{src} = R_{src} + jX_{src} \longrightarrow |Z_{src}| = \sqrt{R_{src}^2 + X_{src}^2} \tag{3.24}$$

The XR_{ratio} is given by:

$$XR_{ratio} = \frac{X_{src}}{R_{src}} \longrightarrow X_{src} = R_{src} \cdot XR_{ratio} \tag{3.25}$$

Combining (3.24) and (3.25) and solving for R_{src}:

$$R_{src} = \frac{Z_{src}}{\sqrt{1 + XR_{ratio}^2}} \tag{3.26}$$

Using (3.25), the source inductance is found:

$$X_{src} = \omega_n L = R_{src} \cdot XR_{ratio} \longrightarrow L = \frac{R_{src} \cdot XR_{ratio}}{\omega_n} \tag{3.27}$$

It was decided to keep $XR_{ratio} = 10$ and manipulate the SCC in (3.24) to change the strength of the external grid. A very strong external grid is represented by a source impedance calculated from $S_{sc} = 10S_b$, while a weak grid is considered to be approximately $2S_B$ or less.

3.4 Virtual Synchronous Machine (VSM) implementation

The Simulink GFM inverter model illustrated in Figure 3.13, will emulate the dynamic behavior of an SG by implementing a digital representation of the swing equation. The GFM consists of two outer control loops: The VSM controller and the PI voltage controller.

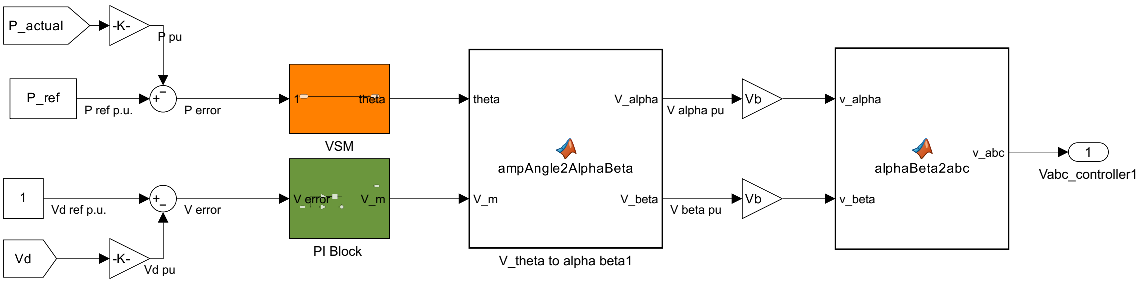

Figure 3.13: Block diagram of the GFM outer loop.

Starting with the VSM, the controller is based on the swing equation:

$$J\frac{d\Omega}{dt} = T_m - T_e \tag{3.28}$$

Where J is the inertia $(Kg\ m^2)$, Ω is the angular speed (rad/s), T_m is the mechanical input torque (Nm), and T_e is the electrical output torque in (Nm). The inertia constant H, which describes the number of seconds the SG can supply the nominal power, is described as:

$$H = \frac{1}{2}\frac{J\Omega_n^2}{S_n} \tag{3.29}$$

Here, Ω_n is the synchronous speed and S_n is the nominal apparent power. Substituting (3.28) into (3.29) yields the following:

$$2H\frac{S_n}{\Omega_n^2}\frac{d\Omega}{dt} = T_m - T_e - D\Omega \tag{3.30}$$

where the additional term $D\Omega$ is the damping constant that is added to further increase the damping effect. Rewriting the equation into per unit and solving for $\frac{d\Omega}{dt}$ leads to:

$$\frac{d\omega}{dt} = \frac{1}{2H}(P_m - P_e - D\Delta\omega) \tag{3.31}$$

This formula expressed in Simulink blocks becomes:

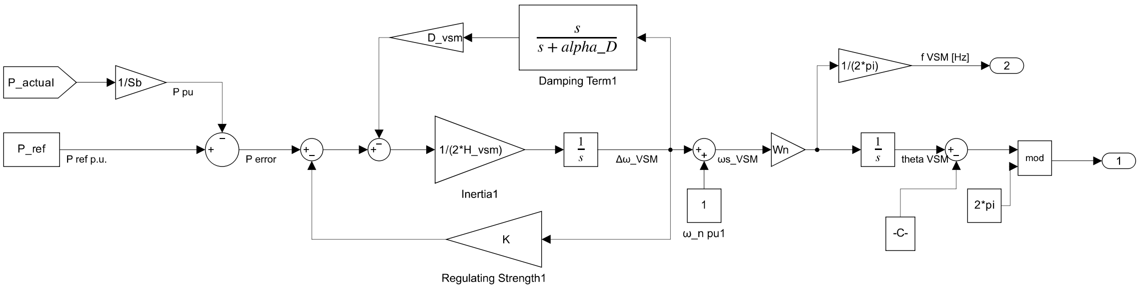

Figure 3.14: Block diagram of the VSM.

A high-pass filter was included for the damping. This was implemented to ensure that the damping is injected only during transients, avoiding continuous power losses in steady-state. Additionally, a droop feedback was included to control the dynamic response as well as ensure proper power sharing with other units. The summation block adds ω_n, ensuring that the VSM output oscillates around the nominal frequency, and the following gain block then converts the p.u. signal to rad/s. The result is then integrated to compute the phase angle δ, which is used to generate the waveform for PWM modulation. An extra constant shown as "-c" was inserted here as well to manually shift the angle. This was due to numerical issues where the voltage waveform from the generator and the inverter was shifted from each other.

In figure 3.15 the block diagram of the voltage magnitude calculation can be seen.

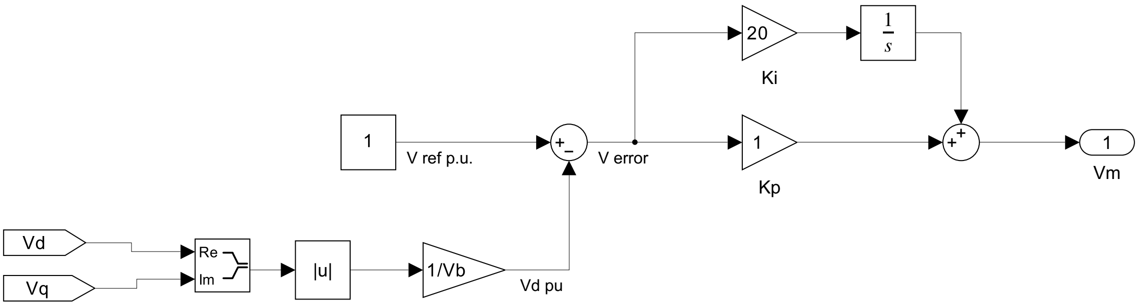

Figure 3.15: Block diagram of the GFM voltage controller.

The magnitude of the voltage is regulated by a PI controller. The reference value is set to 1 p.u. and the actual voltage magnitude is subtracted. In summary, the voltage controller now outputs the voltage magnitude V_m, while the emulated swing equation block outputs the angle δ, and the goal is to transform these into the $V_{abc,ref}$ voltage. These two signals are passed to the ampAngle2AlphaBeta block, which converts the polar form to $\alpha\beta$-coordinates using the formulas:

$$V_\alpha = V_m \cdot cos(\delta) \qquad V_\beta = V_m \cdot sin(\delta). \tag{3.32}$$

The components V_α and V_β are then further passed to the alphaBeta2abc block, which uses the Clark inverse transform (3.33), amplitude-invariant scaling (K = 1), to calculate the three-phase voltage reference $V_{abc,ref}$.

$$\begin{bmatrix} V_a \\ V_b \\ V_c \end{bmatrix} = K \begin{bmatrix} 1 & 0 & \frac{1}{\sqrt{2}} \\ \frac{-1}{2} & \frac{\sqrt{3}}{2} & \frac{1}{\sqrt{2}} \\ \frac{-1}{2} & \frac{\sqrt{3}}{2} & \frac{1}{\sqrt{2}} \end{bmatrix} \begin{bmatrix} V_\alpha \\ V_\beta \\ 0 \end{bmatrix} \tag{3.33}$$

3.4.1 VSM Swing Equation Transfer Function

To evaluate the frequency stability of the VSM, a Bode plot analysis of the emulated swing equation was produced. To achieve this, it was necessary to derive the open loop transfer function of the swing equation used in the simulation. In figure 3.14 the block diagram representation of the swing equation can be seen, where the input of the transfer function is P_{ref} and the output is $\Delta\omega$.

The swing equation of a Virtual Synchronous Machine (VSM) under power imbalance is given by:

$$\Delta\omega(s) = \frac{1}{2Hs}\left[P_{\text{ref}}(s) - K \cdot \Delta\omega(s) - D_{\text{vsm}} \cdot \frac{s}{s+\alpha_D} \cdot \Delta\omega(s)\right] \tag{3.34}$$

Bringing all $\Delta\omega(s)$ terms to the left-hand side:

$$\left(2Hs + K + D_{\text{vsm}} \cdot \frac{s}{s+\alpha_D}\right) \cdot \Delta\omega(s) = P_{\text{ref}}(s) \tag{3.35}$$

Final transfer function:

$$\frac{\Delta\omega(s)}{P_{\text{ref}}(s)} = \frac{1}{2Hs + K + D_{\text{vsm}} \cdot \dfrac{s}{s+\alpha_D}} \tag{3.36}$$

4

Results

This chapter presents a dynamic performance and stability analysis of the systems. This includes step response evaluations, stability margins, and the impact of grid SCC on PLL performance.

4.1 Verification of controllers

The performance of the implemented control loops was evaluated according to the procedure described in section (3.1.4). Step response tests were conducted for the power controller, current controller, PLL, and the results are presented below. In addition, a performance test was carried out for the water turbine to verify that it worked. The results from this test are shown later in Figure 4.18.

4.1.1 Step Response - Current controller

Figure 4.1 presents the step response of the current controller in the GFL inverter. The input step occurs at $t = 1$ s and goes from 0 $p.u.$ to 0.1 $p.u.$. The maximum overshoot of the output is approximately 0.108 $p.u.$. This corresponds to an overshoot of $M = 8$ % (3.8) relative to the steady state value. This arises due to aggressive proportional and integral gains in the PI controller as there is delay caused by sampling and converter switching. Although overshoot is generally not desired, this design choice is acceptable in this case as the current controller is significantly faster than the outer power control loop. The time constant (63 % of the steady state value, equation 3.7) was found to be approximately 1.8 ms.

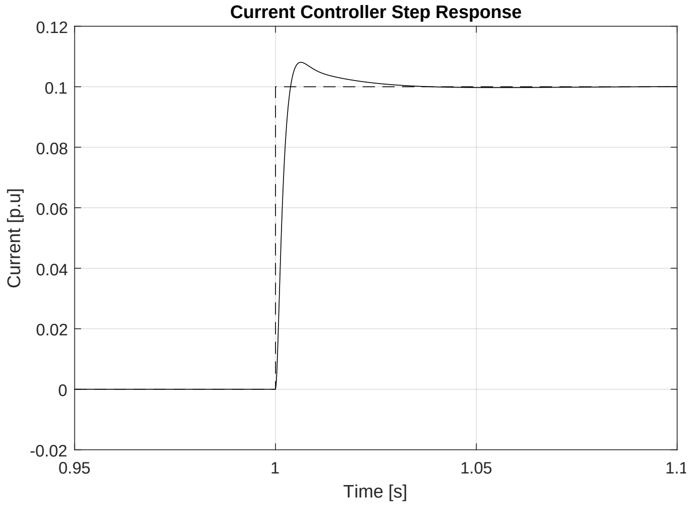

Figure 4.1: Step response of the current controller. The solid line shows the measured I_d, and the dotted line represents the reference $I_{d,\text{ref}}$.

4.1.2 Step Response - Power controller

Figure 4.2 presents the step response of the power controller in the GFL inverter. The input step occurs at $t = 1\ s$ and goes from 0 $p.u.$ to 0.1 $p.u.$. The response of the output shows an initial rapid increase to around 0.05 $p.u.$, followed by a smooth rise toward a steady state. The time constant was found to be approximately 32 ms, which corresponds to a ratio of 17 between the current and the power controller. Thus, the system satisfies the requirement of an inner loop at least 10 times faster compared to the outer loop.

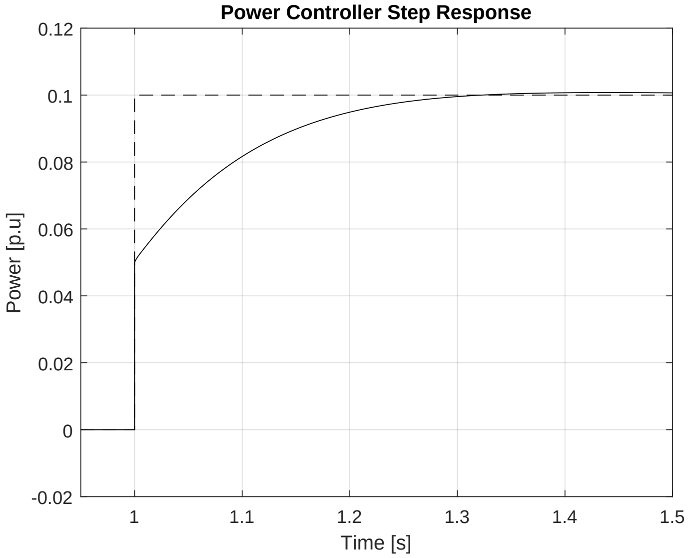

Figure 4.2: Step response of the power controller. The dotted line represents the reference active power P_{ref}, while the solid line shows the actual output power P.

4.1.3 Step Response - PLL

The last response, shown in Figure 4.3, shows that the PLL follows a first-order response without any overshoot. The input step, which is a frequency deviation, occurs at $t = 6\ s$ and goes from 0 $p.u.$ to 0.1 $p.u.$. A frequency deviation of 0 p.u. indicates that the grid frequency is operating at 50 Hz. The time constant is approximated to be 72 ms, which means that the total time constant for the GFL inverter, that is the current controller, power controller, and PLL is approximately 106 ms.

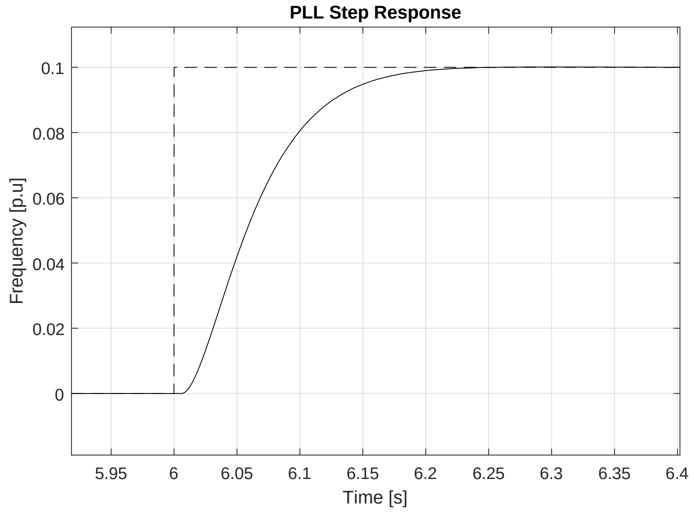

Figure 4.3: Step response of the PLL controller, showing a first-order behavior with no overshoot. The dotted line represents the reference input signal, while the solid line shows the step response.

4.2 Stability margins

In this section, the stability of the different systems operating under various conditions is examined. The focus is on how the filter time constant τ and the proportional gain K_h influences the stability region for different methods, which are low-pass, moving average, and pure delay, given as:

Low pass filter: $H(s) = \dfrac{1}{\tau s + 1}$

Moving average: $H(s) = \frac{1-e^{-s\tau}}{s\tau}$
Pure delay: $H(s) = e^{-s\tau}$

Plotting the Bode-diagrams for the low-pass filter and the moving average

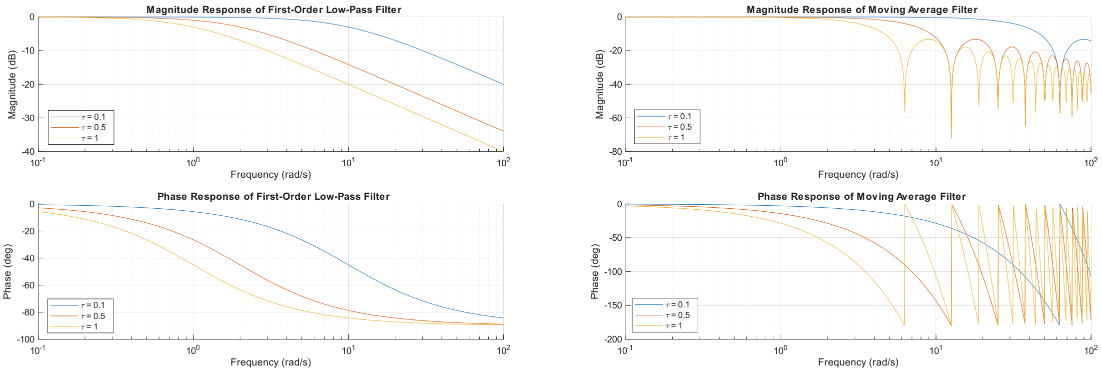

(a) Magnitude response of LP filter

(b) Magnitude response of moving average filter

Figure 4.4: Bode-plots of low-pass and moving average filters.

we can see that the responses are different from each other as well. In Figure 4.4a, the magnitude and phase response of the LP filter for three different time constants is shown, while in Figure 4.4b the corresponding response of a moving average. The LP filter shows a much more smooth response as the frequency increases, while the moving average displays a response where with periodic passbands that could lead to undesirable behavior for the control system.

Results from the time-domain simulations are also included to illustrate how the instability affects the system when operating outside the stability boundaries.

4.2.1 GFL - External grid - FFR

The first case for the stability analysis included the GFL inverter connected to an external grid with variable strength operating in FFR mode. The control system included current, power, and PLL controllers, as illustrated in the control diagram provided in Figure 2.2. A frequency deviation of -2 Hz/s for 1 second followed by 2 Hz/s for another second was programmed into the controllable voltage source. The range ± 2 Hz/s was chosen based upon EIFS-2018-2 requirements in [37] . This case was used for all controller configurations to ensure full activation of the active power output, making each test comparable. It is not a realistic frequency deviation, it is rather an extreme case used to properly display the behaviour of the controller strategy. The range of the power controllers proportional gain used was decided to be 25-500. Where 25 corresponds to a 1 p.u. active power output when the frequency deviates 2 Hz, and 500 corresponds to a 1 p.u. active power output when the frequency deviates 0.1 Hz. All filters, applied in the power controller after the frequency error has been calculated, were then tested for filter time constants ranging from 0-1 seconds.

In Figure 4.5 the active power injected into the grid from the GFL inverter based on the frequency deviation can be seen. The SCC of the external grid is 50 MVA, while the inverter is 10 MVA, and the figure presents the toughest case in the FFR mode.

The proportional gain is 500. The filter time constant is 1 second, corresponding to a very long system delay. As can be seen in the graph, the stability of the system is maintained. Due to the long time constant the GFL inverter is injecting active power for several seconds after the disturbance has been cleared, which would not be desirable in a real case.

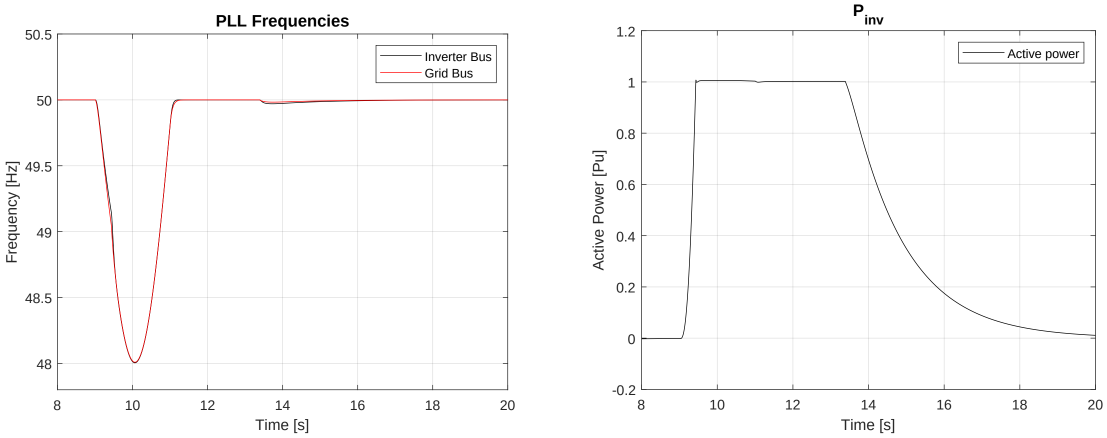

(a) PLL measured frequency **(b)** Active power from GFL inverter

Figure 4.5: GFL inverter in FFR mode - External grid at 50 MVA

Figure 4.6 presents the same GFL inverter setup as previously with a modified external grid SCC, which in this case is 13 MVA. It can be seen that the PLL tries to maintain synchronism with the grid but quickly becomes unstable, leading to rapid oscillations throughout the system. These oscillations are likely occurring because the large impedance connected to the external grid causes distortions in the voltage phase and amplitude during power injections, which the PLL simply misinterprets, and the measurement becomes faulty. After testing, approximately 13 MVA seen as the limit for when the GFL inverter would become unstable. These results show that the GFL inverter can maintain stability and synchronism with the grid, while providing aggressive FFR with high filter constants, as long as the external grid is at least 1.31 times stronger than the inverter.

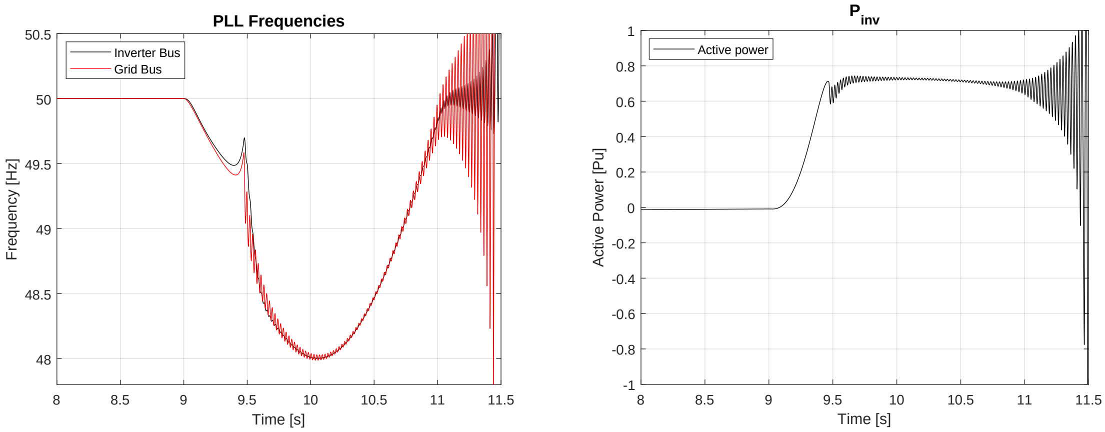

(a) PLL measured frequency **(b)** Active power from GFL inverter

Figure 4.6: GFL inverter in FFR mode - External grid at 13 MVA

Figure 4.7 displays the GFL inverter in FFR mode with a much less aggressive setup. The proportional gain is 25, which corresponds to full active power injection at a frequency deviation of ±2 Hz. The filter time constant is 0.1 seconds, corresponding to a short system delay. It can be seen that, similar to the previous case, the system can not maintain stability under these conditions. These results show that the strength of the external grid is the main factor to consider when providing FFR from a GFL inverter.

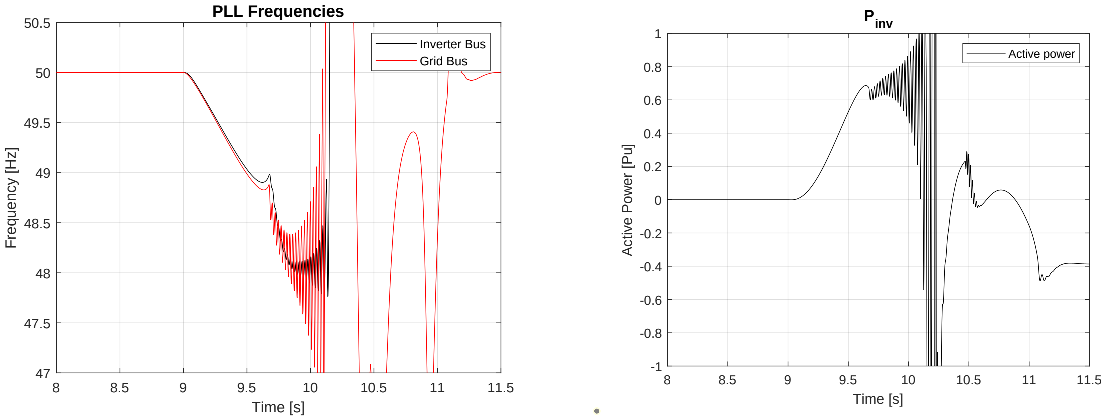

(a) PLL measured frequency **(b)** Active power from GFL inverter

Figure 4.7: GFL inverter in FFR mode - External grid at 12.5 MVA

The results showed that if the grid strength were kept constant, there was no configuration in proportional gain or filter time constant that could move the inverter from stable to unstable, or the other way around. The resulting stability margins of the GFL inverter operating in FFR mode can be seen in figure 4.8.

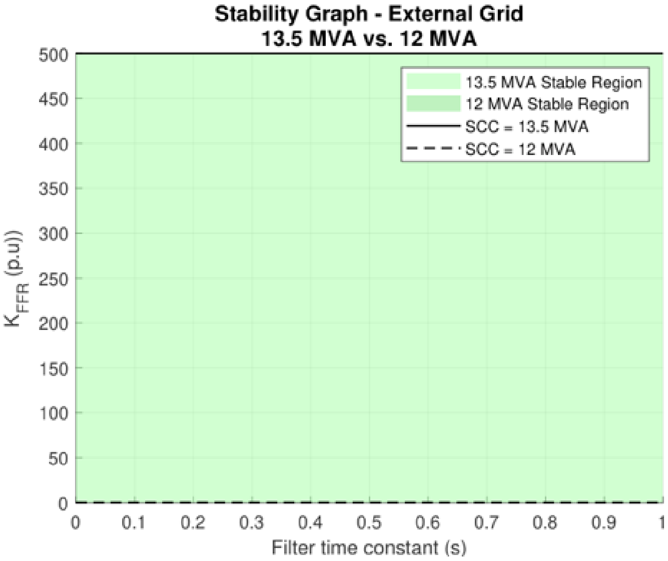

Figure 4.8: Stability graph of externally connected GFL operating in FFR.

Three different filtering methods were tested, LP filter, moving average filter and a pure delay. None of them could affect the stability margin. In the figure it can be seen that if the external grid strength was greater than 13.5 MVA, the GFL inverter would remain stable. The proportional gain was tested up to a value of 50000, with a time constant of 1 second, which resulted in stability with a grid strength of 30 MVA. The only variable that affected stability was the strength of the external grid, where the limit was found at 13.5 MVA.

4.2.2 GFL - External grid - Synthetic inertia

In figures 4.9 and 4.10 the stability range of a GFL inverter with different filtering methods that provide synthetic inertia to a strong external grid is shown. In both cases, the y-axis is represented by the RoCoF gain in $p.u/(Hz/s)$ (3.21) and the x-axis is represented by the filtering time constant, τ, in seconds. All tests were carried out with two different levels of external grid strengths, 50 MVA and 30 MVA. In Figure 4.9 the GFL inverter utilizes low-pass filtering after the RoCoF measurement.

It can be seen that the RoCoF gain and filtering have a linear relationship. As the gain increases for the GFL inverter to be able to output the same amount of active power for a smaller disturbance, the filtering must increase to smooth the high-frequency signals. When the strength of the external grid decreases, so does the RoCoF gain for a given time constant.

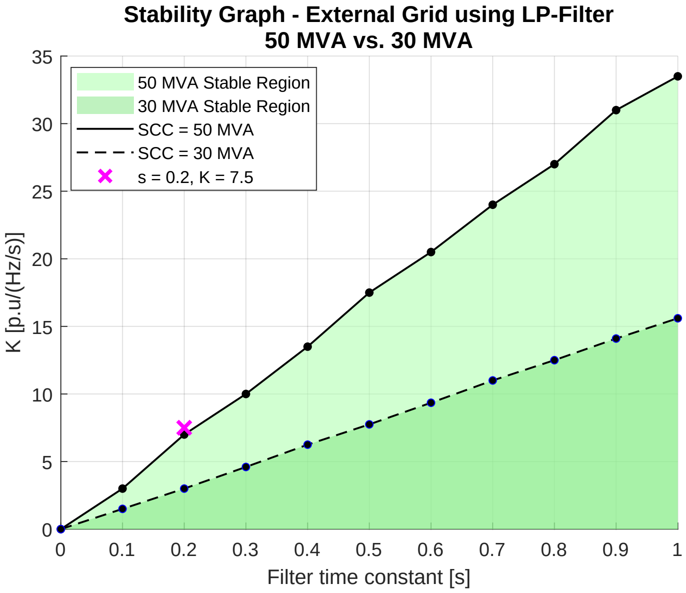

Figure 4.9: Stability boundary of a GFL inverter with a low-pass filter providing synthetic inertia

Therefore, in order for the GFL synthetic inertia inverter to be more aggressive, more filtering (also making the GFL slower) was needed to filter out the high-frequency components.

In Figure 4.10 the GFL inverter utilizes a moving average filter after the RoCoF measurement. Initially, the relationship between the RoCoF gain and the filter time constant is linear and similar to the previous case with a low-pass filter. However, as the filter time constant increases above 400 milliseconds, the stability region drastically decreases. The performance of the GFL inverter as the strength of the external grid decreases is identical to the previous case. If the external grid is weak, the GFL inverter can not provide as much synthetic inertia.

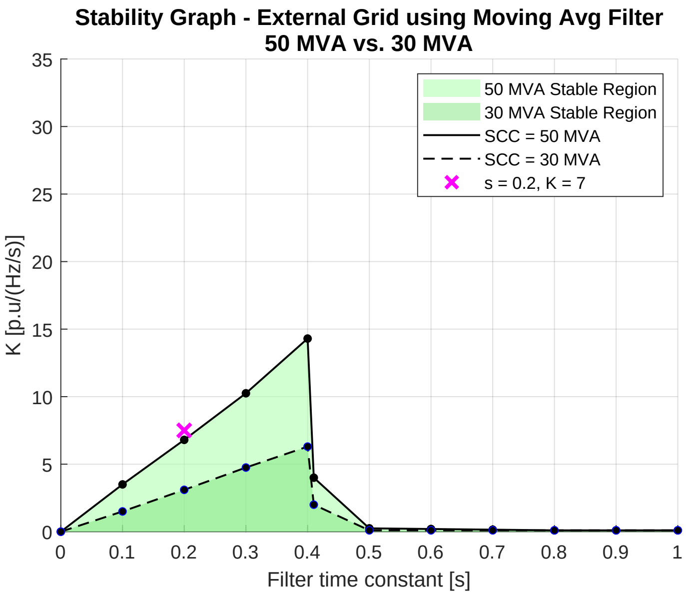

Figure 4.10: Stability boundary of a GFL inverter with a moving average filter providing synthetic inertia

A third case was tested where the frequency derivative was passed through a pure delay function. It was observed that the system could not maintain stability even with the shortest delay possible. The delay function was removed; however, the GFL inverter was unable to maintain stability. These results showed that to use the GFL inverter for synthetic inertia production filtering has to be included.

In Figure 4.11 two cases where the GFL inverter could not maintain stability are shown. The graphs show the active power regulation current I_d in the inverter. Figure 4.11a presents the case where the RoCoF measurement is passed through a low-pass filter. With a gain RoCoF gain of 7.5 and a filter time constant of 200 milliseconds, the configuration lands outside of the stability region in Figure 4.9. The result is a fast oscillation in I_d of approximately 120 Hz, propagating throughout the system with a slight increase in amplitude.

Figure 4.11b presents the second case in which the RoCoF measurement is passed through a moving average filter. The RoCoF gain is equal to 7 and the filter time constant is equal to 200 milliseconds, which corresponds to a point outside the stable region in Figure 4.11b. This configuration results in a rapid oscillation of approximately 100 Hz with variable amplitude.

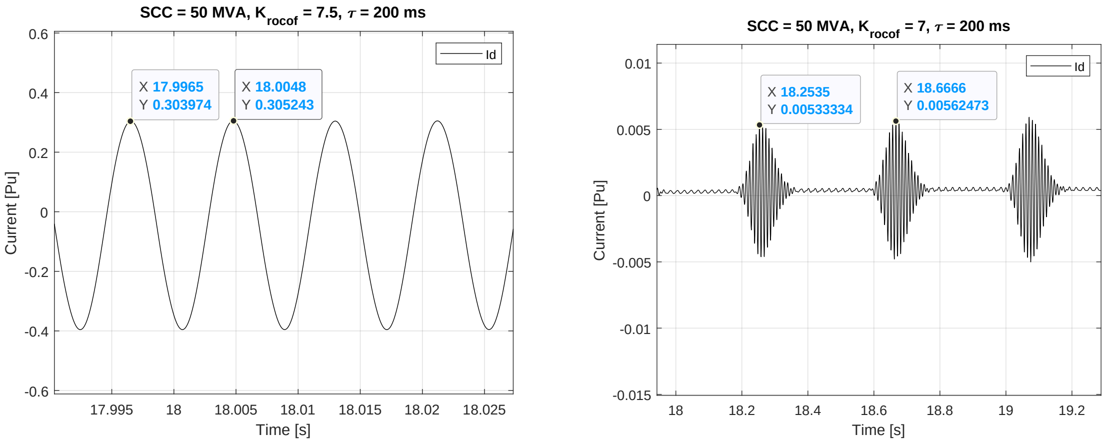

(a) Low-pass filter **(b)** Moving average filter

Figure 4.11: System oscillation as a result of too high RoCoF gain

Figure 4.12 shows the voltage, V_q, at the inverter bus during a frequency disturbance. The GFL inverter is set to synthetic inertia, the proportional RoCoF gain is 1 and the low-pass filter time constant, τ, is 500 milliseconds. The strength of the external grid is swept, starting with a strong grid of 100 MVA and ending with a weak grid of 13 MVA. It can be seen that a weaker grid results in a high frequency oscillation in V_q, which represents the quadrature component of the voltage at the PCC and is directly related to the phase angle of the voltage.

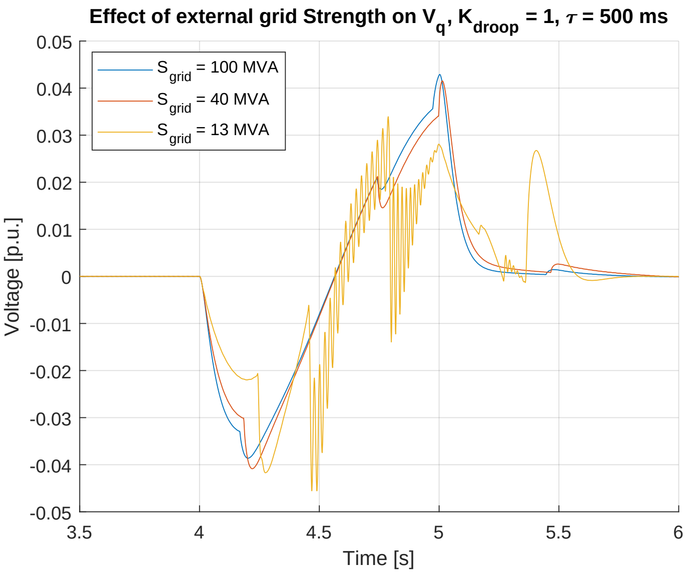

Figure 4.12: V_q during disturbance at different external grid strength

Because the simulation was performed with an EMT model, it was possible to see this 50 Hz oscillations. These kinds of fast oscillations would not show up in a RMS model and therefore explains the reason why the system was modeled as EMT.

The observed poorly damped, resonance-like behavior is consistent with Control Interactions between a Device and Network (CI-N), a phenomenon commonly associated with power electronic systems. While CI-N is typically linked to subsynchronous oscillations at lower frequencies, the oscillations here occur near 50 Hz, suggesting that weak grid conditions and insufficient damping are more likely the root causes. Similar cases have been reported in wind farms, where fast control-loop dynamics combined with weak grids leads to oscillation [38], [39]. Mitigation strategies for such interactions are discussed also in [40], where it is shown that enhancing the inner current control or upgrading the PLL can significantly reduce oscillation. As highlighted in the paper, PLL bandwidth and design are crucial in regards to the interaction between the inverter and weak AC grid and this could also be the cause in this simulation.

4.2.3 GFL - Island grid - FFR

Figure 4.13 illustrates the stability region for a GFL inverter operating in island mode. As previously described, the horizontal axis represents the filter time constant, while the vertical axis shows the gain K_{FFR}. The stability boundaries for three different filters are plotted: the low-pass filter (solid black), the moving average filter (dashed blue), and the time delay (dash-dot in red). Two cases where the parameter combination lies just outside the stable region are also plotted with purple crosses.

The graph indicates that the low-pass filter provides the largest stability margin across the entire range, followed by the moving average filter, and with the time delay being the least stable.

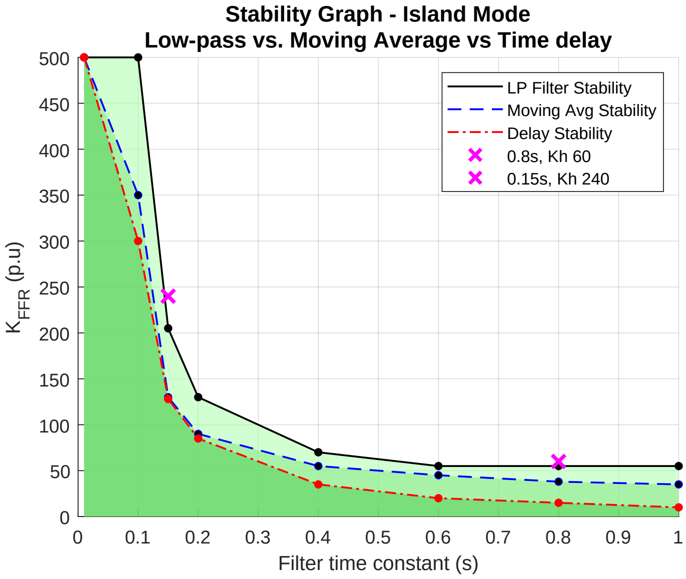

Figure 4.13: Stability boundaries for a FFR operating GFL in an island grid, plotted for three types of filters. The purple crosses indicate two parameter combinations that are outside the stable region.

The first unstable case, shown in Figure 4.14, corresponds to a filter time constant of 0.8s and a gain of $K_{FFR} = 60$. Here, the system shows a low oscillating frequency with a relatively large amplitude in both the generator and PLL frequencies. The oscillation of the frequency is approximately 0.35 Hz and the amplitude reaches up to ± 2 Hz within 14 seconds. The PLL frequency also appears to be slightly phase-shifted behind the generator frequency but otherwise tracks the waveform well.

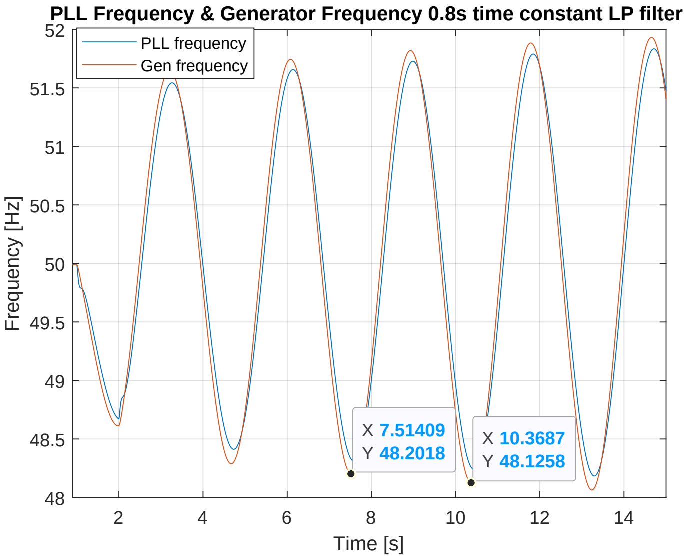

Figure 4.14: After fault PLL and generator frequency for a low-pass filter with time constant 0.8 s and gain $Kh = 60$.

In the second case, illustrated in Figure 4.15, the system is now configured with a shorter time constant of $0.15s$ and a higher gain of $Kh = 240$. This results a in faster, oscillations of approximately 0.74 Hz and a smaller amplitude oscillating at around ± 0.5 Hz within 14 seconds. Unlike the previous case, the PLL now performs noticeably worse at tracking the generator frequency accurately, showing large deviations during both high and low peaks.

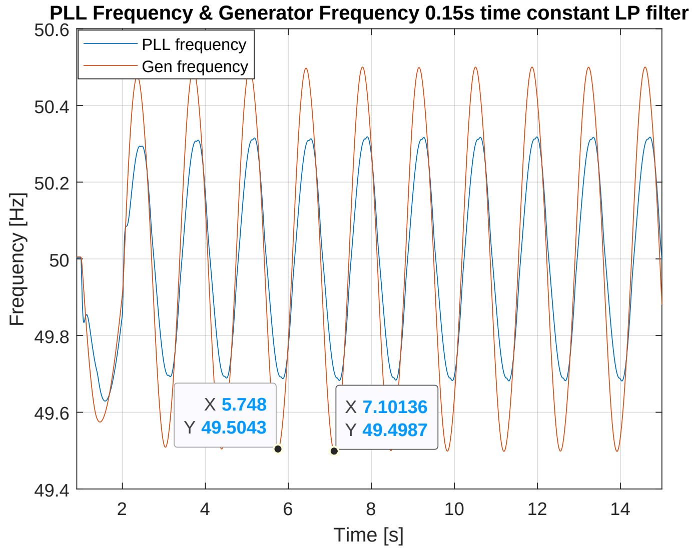

Figure 4.15: After fault PLL and generator frequency for a low-pass filter with time constant $0.15s$ and gain $Kh = 240$.

4.2.4 GFL - Island grid - Synthetic inertia

The results from the Island grid simulations with synthetic inertia implemented in the GFL are presented in 4.16.

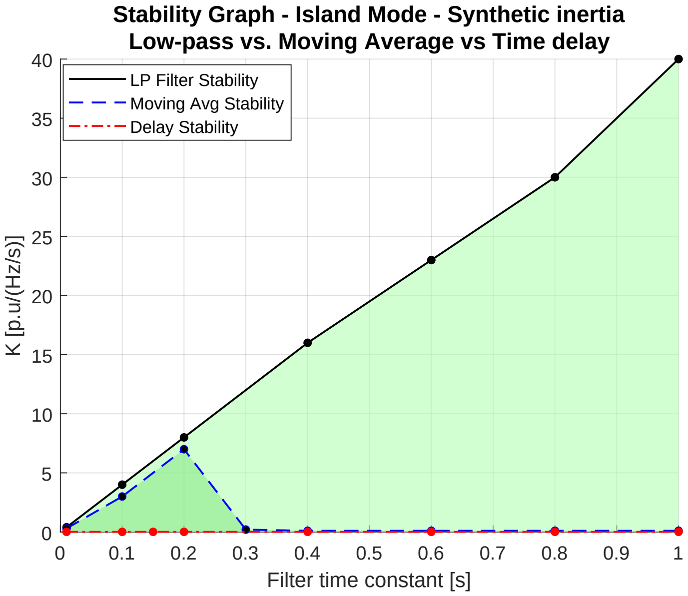

Figure 4.16: Stability boundaries for a synthetic inertia operating GFL in an island grid, plotted for three types of filters.

Similarly to the external grid case observed earlier, the relationship between the synthetic inertia gain and the filter time constant shows an approximately linear behavior with the low-pass filter used. As the gain increases, a greater filtering time constant is required to maintain system stability.

The stability characteristics of the moving average filter were also consistent to the external grid. In both cases, the system remained stable as the time constant and the gain increased linearly up until a certain point where instability rapidly occurred. In the island operation however, this turning point occurred earlier at a smaller time constant around 0.2-0.3 s compared to the external grid at around 0.4 s.

The moving average filter, as illustrated earlier in the bode plot (4.4), showed non-linear magnitude and phase behavior. Unlike the low-pass filter, the moving average introduces notches in the frequency response, by sharp phase shifts (visualized as jumps due to wrapping). As the filter windows τ increases, these notches and the associated phase lags shift towards lower frequencies. Therefore not only affecting the high-frequency components but also the system's dynamics. This could be the reason for the resulting instability in the synthetic inertia response as it was seen to be more sensitive compared to the FFR strategy.

For the time delay case, all tested time constants within the range of 0-1 s led to system instability. To further investigate this, the measured RoCoF before and after filtering was plotted in an unstable case, shown in Figure 4.17.

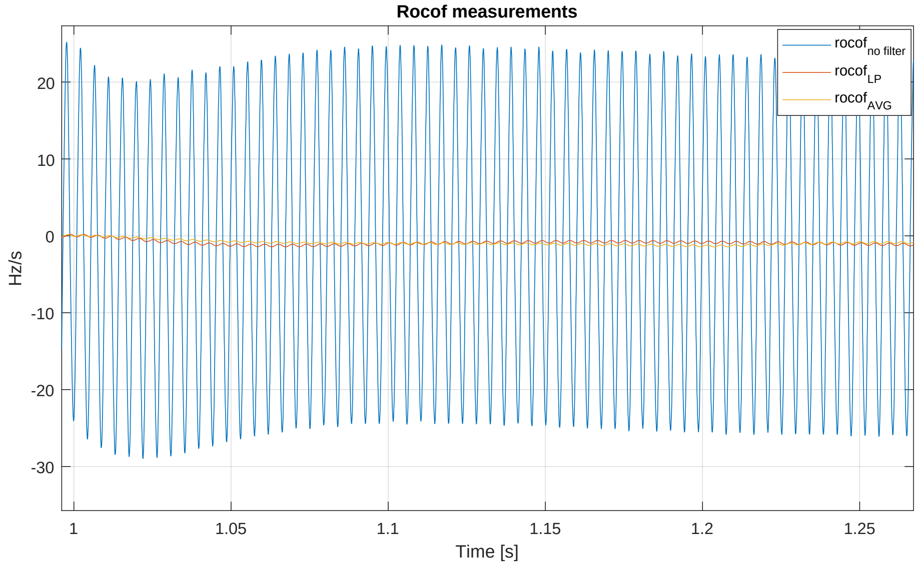

Figure 4.17: Rocof measurements before and after filtering

As observed in the case without any filtering / 0 s delay (the blue curve), the RoCoF measurement showed a large high-frequency oscillation at approximately 230 Hz. This shows that the built-in filtering provided by the PLL is not sufficient to the suppress high-frequency components in this scenario and therefore a pure delay cannot be tested alone.

Also, compared to the FFR case, this stability plot showed the opposite behavior between gain and filtering time constants. One possible explanation is due to the RoCoF estimation that introduced such high-frequency components, thus leading to instability for the synthetic inertia case for low filtering applied.

4.3 GFL - FFR vs. Synthetic Inertia comparison

In the previous section, the stability margins for the various control strategies were shown and cases where the system was unstable. In this section, the FFR and synthetic inertia control strategies are evaluated for a stable case, with a filter time constant of $\tau = 0.2s$ and maximum gain applied according to the stability margins, for a grid disturbance of 2Hz/s for 1s that occur at 1s and disappears at 2s. That is, a gain of $K_h = 8$ for the synthetic inertia and a gain of $K_h = 140$ for the FFR- Figures 4.18 to 4.20 show the system's power and frequency inertial response for the three different configurations, in all cases, the system reached steady state.

In Figure 4.18, the results from the island grid without any GFL inverter connected are shown. In Figure (a), the generator frequency drops significantly following the disturbance of a large load increase ($P_{step} = P * 1.6$) , reaching a frequency nadir of approximately 48 Hz. This corresponds to a RoCoF of 2 Hz/s, which was set as the grid disturbance. In Figure (b), it can be seen that the SGs active power (P_e) instantly reacts to the disturbance (due to the inertia) as the mechanical power (P_m) initially drops as the pressure in the waterways drops. The system in this case solely relies on the SGs to uphold the frequency, however because the inertia is used to inject active power, the rotor will slow down. As the frequency is directly proportional to the rotor speed, the frequency will fall as well, resulting in a deep nadir.

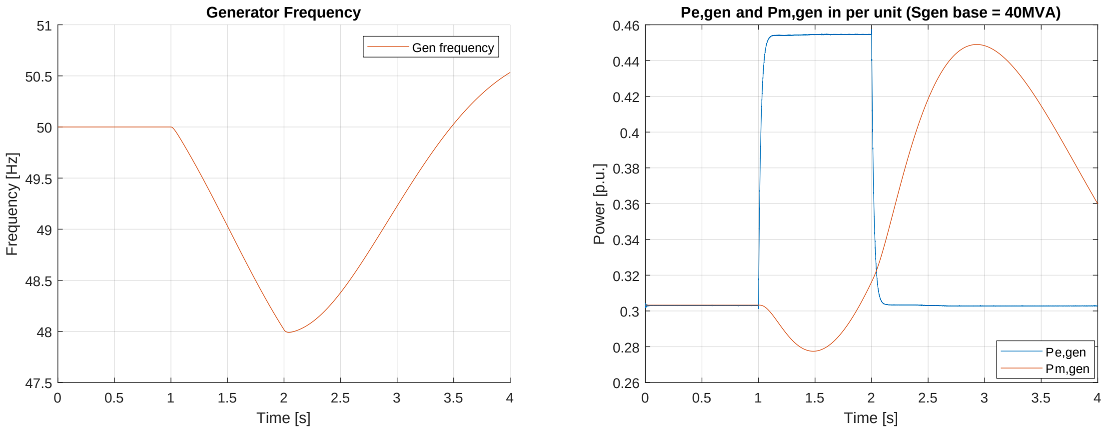

(a) Generator measured frequency.

(b) Active power from SG.

Figure 4.18: Island grid, no GFL connected

In Figure 4.19, the system is now equipped with a GFL inverter operating in FFR mode. In Figure (a), it can be seen that the frequency dip is partly mitigated compared to the previous case, with the frequency nadir reaching around 49.3 Hz. The PLL tracks the generator frequency with some delay and deviation, but still manages to follow the overall trend of the curve. In Figure (b), the inverter begins slowly to inject active power, reaching 1 p.u. (0.25 p.u. of SG) of its nominal power at around 2 seconds.

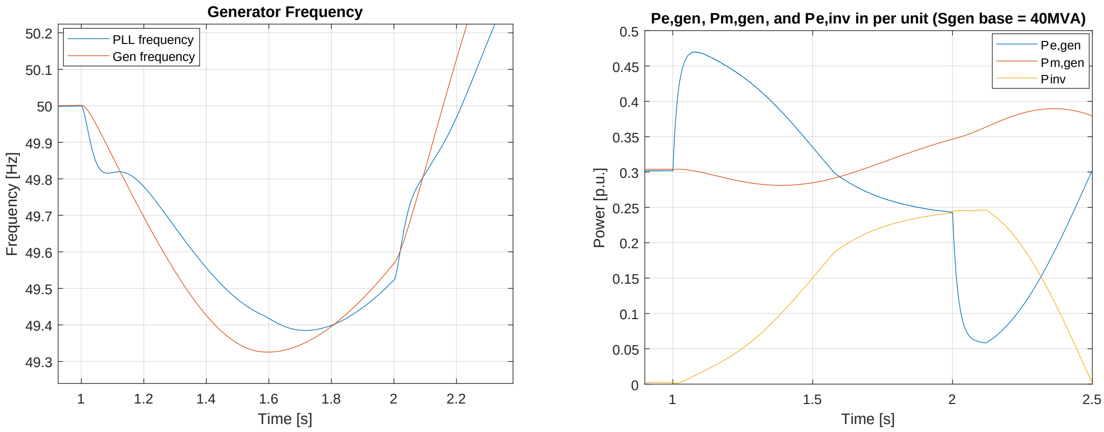

(a) PLL and SG measured frequency **(b)** Active power from GFL and SG.

Figure 4.19: Island grid, GFL inverter in FFR mode

Lastly, in Figure 4.20, the results from GFL operating with a synthetic inertia control strategy are shown. In Figure (a), the plot shows the SG and PLL frequency where the generator shows clear oscillation and reaches a lowest frequency of roughly 49.85 Hz as the PLL struggles to track the SG frequency. In Figure (b), the active powers from both units are shown. The inverter now responds significantly faster to the fault compared to the FFR case, reaching a peak output of approximately 0.9 p.u. of its nominal power (equivalent to 0.22 p.u. of SG), around 1.4 seconds after the disturbance.

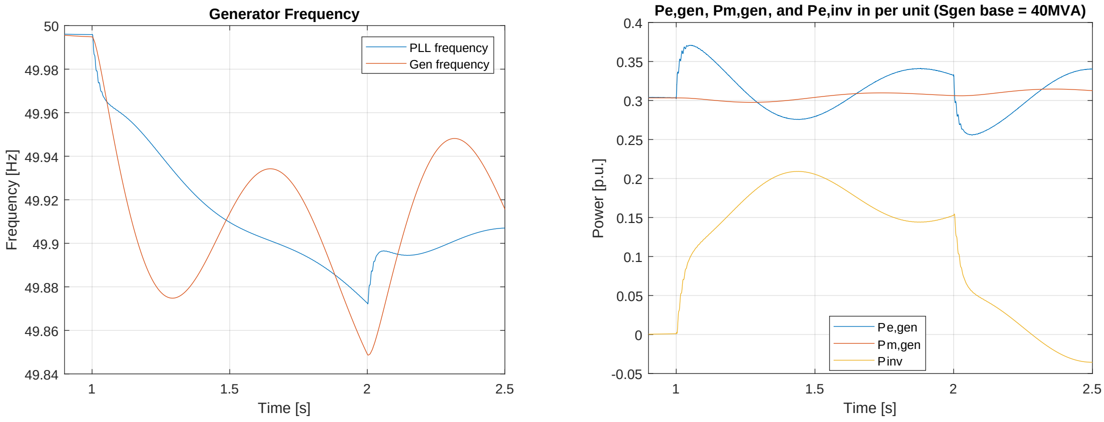

(a) PLL and SG measured frequency **(b)** Active power from GFL inverter

Figure 4.20: Island grid, GFL inverter in Synthetic inertia mode

Despite the difference in control strategy, the results show that both the FFR and synthetic inertia injected a similar amount of active power to the system during the disturbance. This means that the control strategies can be compared against eachother fairly.

4.4 GFM - VSM

To evaluate the behavior of the VSM, simulations were performed in the island grid where parameters such as the inertia constant, damping coefficient, high-pass filter time constant, and droop constant were varied, as discussed in 3.4. Among these, the droop constant was found to have the most significant influence on system stability. Figures 4.21 to 4.23 illustrate the results of three different droop settings, 4%, 2%, and 1%. The system was subjected to a load step at 2 seconds, corresponding to a 2 Hz/s RoCoF for 1 second, until the load decreased again. It can also be seen that then system for all cases are small-scale oscillating pre-disturbance, this is numerical due to the fact that the simulation did not start completely in steady state at 0s.

With a droop setting of 4%, the hydropower and the VSM inverter's active power output began to oscillate against each other. This led to unstable behavior with increasing oscillations until the system ultimately loses synchronism. The frequency of the oscillations was measured to be approximately 1.6 Hz.

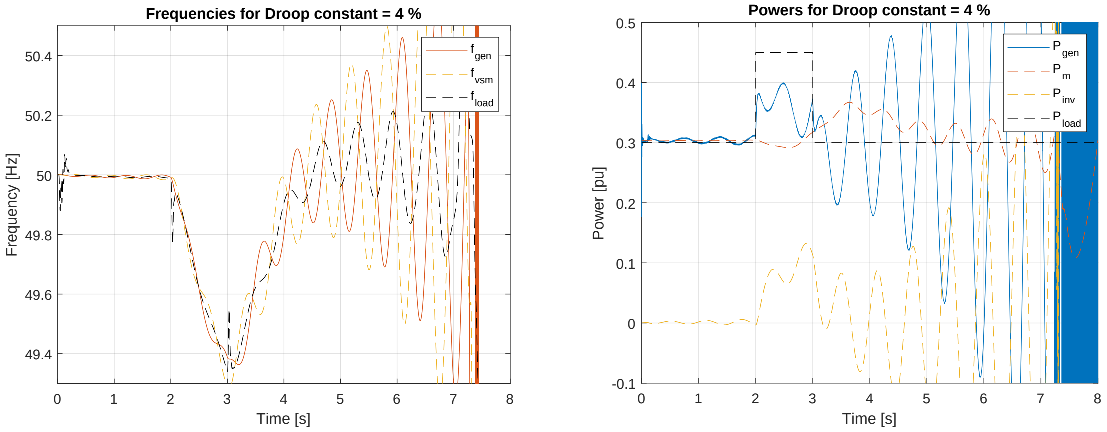

(a) Measured frequency

(b) Active power from Hydropower and VSM

Figure 4.21: VSM results with a droop of 4%.

In the second case, with a droop constant of 2%, both the frequency and power outputs continue to exhibit oscillations of similar characteristics as in the previous case at 1.6 Hz. However, the system does not show increasing oscillations and instability within the given time frame. The VSM inverter output power reaches a peak of approximately 0.14 system p.u. (equivalent to 0.56 p.u of the inverter).

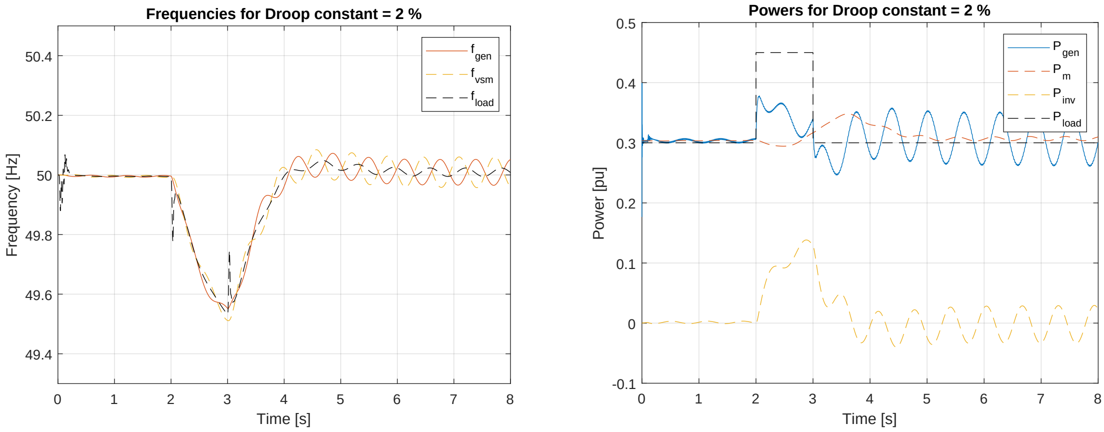

(a) Measured frequency

(b) Active power from Hydropower and VSM

Figure 4.22: VSM results with a droop of 2%.

In the third and final scenario, with a droop constant of 1%, the system exhibits a damped response where the frequency successfully returns to the nominal value after the load is reduced. The frequency nadir reaches ≈ 49.72 Hz during the disturbance, and the inverter outputs 0.15 p.u. after one second.

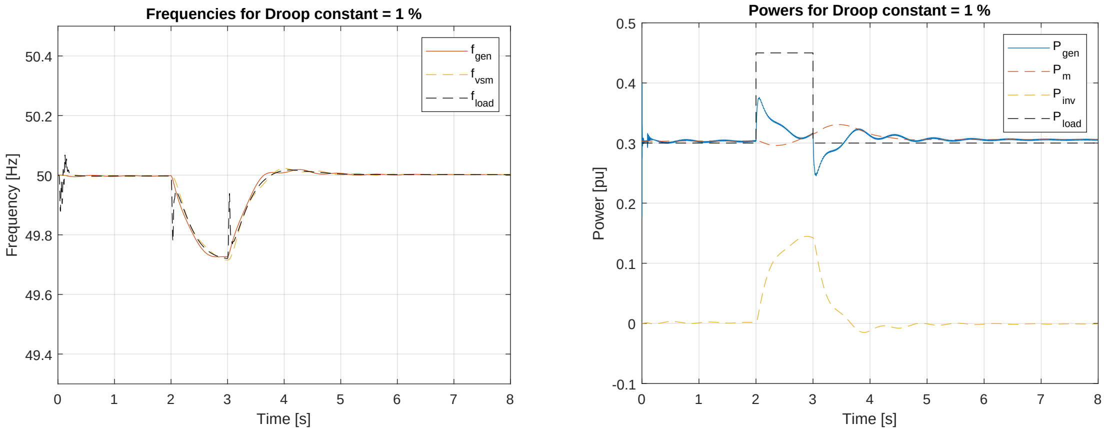

(a) Measured frequency

(b) Active power from Hydropower and VSM

Figure 4.23: VSM results with a droop of 1%.

In Figure 4.24, the Bode plot analysis of the emulated swing equation is presented. As explained in the implementation of the VSM, the input of the transfer function is P_{ref} and the output is $\Delta\omega$. From the magnitude plot it can be seen that the system includes a steady state gain. This is from the regulating strength, droop, of the VSM. The regulating strength of the VSM is calculated as the inverse of the droop, for example, a droop $R = 1\%$ equals the regulating strength $K = 100$. In dB, this becomes:

$$20\ \log_{10}(R)\ =\ 20\ \log_{10}(0.01)\ = -40\ dB \tag{4.1}$$

From the phase plot it can be seen that for a decreasing droop constant, the phase lag decreases. The combination of increasing gain and decreasing phase lag is an important relationship with respect to the stability of the VSM.

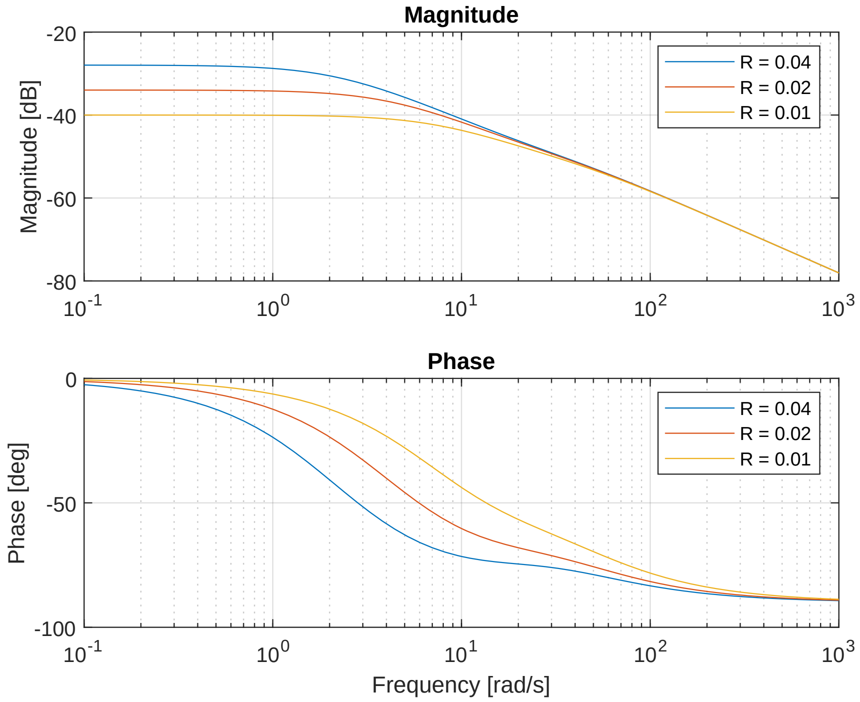

Figure 4.24: Bode plot of swing equation in VSM with variable regulating strength.

4.5 PLL Operation - Phase Shift

The final tests covered the ability of the PLL to track the frequency of the grid during phase jumps. The phase jump was programmed into the controllable voltage source. At 8 seconds, the phase angle shifted -30 degrees and at 14 seconds, it shifted +30 degrees, as seen in figure 4.25. The GFL inverter is operating in synthetic inertia mode, connected to the external grid. The proportional gain is 10, corresponding to a 1 p.u. active power output when the RoCoF is ± 0.1 Hz/s, and the low-pass filter time constant is 0.3 seconds.

When the phase shift occurs, the frequency deviates sharply from its steady state. This is to be expected, as the phase jump introduces a transient frequency deviation. As the strength of the external grid decreases, it takes a longer time for the PLL converge back to 50 Hz. However, the amplitude of the frequency measurement is greater when the external grid is stronger.

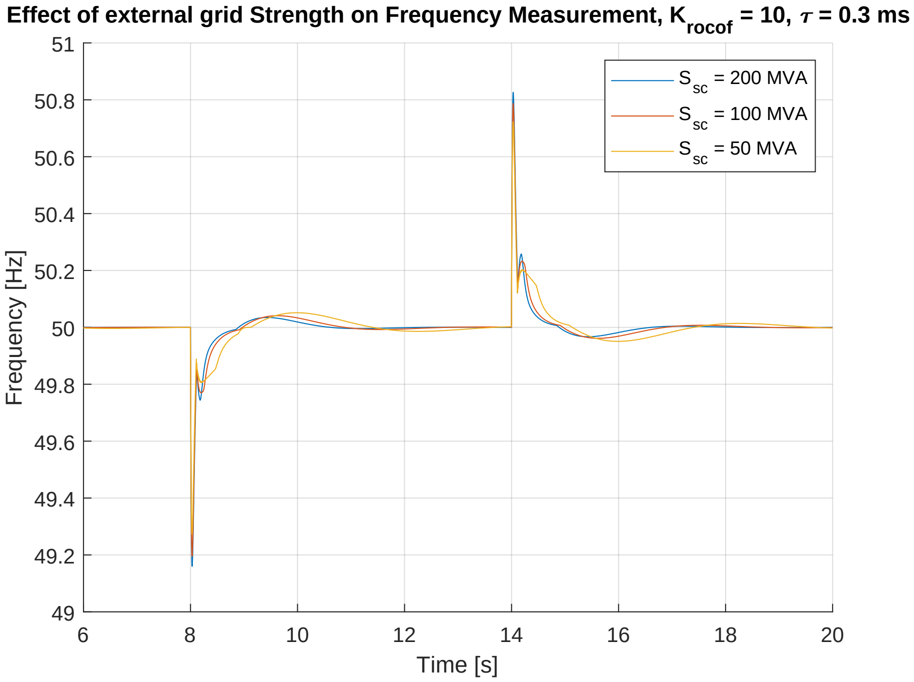

Figure 4.25: PLL frequency during phase shift with variable grid strength.

The GFL inverter was able to maintain stability at lower external grid strengths, with the same configuration, compared to the case in section 4.2.2. This is likely due to the phase angle jump not being as severe of a disturbance as the frequency deviation. However, if the external strength is low enough, the PLL is unable to track the phase angle of the voltage, resulting in instability.

5

Discussion

This chapter will interpret the results of the study. It will provide a discussion of why the results are relevant, what the potential is, and what limitations there might be. This will include analyzing the impact of different system variables in GFL and GFM inverters, such as proportional gain, filter time constants, and the strength of the external grid.

5.1 GFL - FFR & Synthetic inertia - External grid

When operating the GFL inverter in FFR mode, a key finding was that the strength of the external grid appeared to be the dominant factor for the inverter control system to be able to maintain stability. If the GFL inverter provided frequency support to a strong external grid (e.g. $5 \cdot S_{B,INV}$), it would maintain its stability even with extremely aggressive and challenging settings. However, as the strength of the external grid weakened, the GFL inverter, particularly the PLL, would lose synchronism with the grid. The results showed that at an external grid strength below $1.3 \cdot S_{B,INV}$ the inverter could no longer maintain stability. This behaviour is expected since it is known that PLLs tend to lose synchronism while tracking a weaker grid frequency. The observations also align with expectations as a stronger grid would offer a better and more rigid voltage and frequency signal, which is less prone to oscillations.

In the case of operating the GFL inverter in synthetic inertia mode, i.e. injecting active power based on RoCoF, it was seen that the filtering method would greatly affect the stability margins. At lower proportional gain and filter time constants, the low-pass filter and moving average filter showed similar behavior with a linear increase in stability margin. However, when the filter time constant increased above 400 milliseconds, the moving average filter displayed a rapid drop in stability margin. This behavior occurs when the RoCoF signal becomes too delayed. The controller tries to adjust its output based on a faulty measurement. This can cause a feedback loop that reinforces the oscillations in the system. It can be seen that even the smallest proportional gains can not maintain stability when the delay is too great.

These results further highlight the importance of proper filtering when providing synthetic inertia to ensure stable operation. Both filtering methods behaved similarly when the strength of the external grid decreased; the stable region decreased.

This is, as mentioned above, an expected behavior, since a weaker external grid is not able to dampen oscillations as effectively as a stronger one.

5.2 GFL - FFR & Synthetic inertia - Island grid

From the simulations, it was seen that both the synthetic inertia and FFR implementations in the GFL inverter were fully functional and helped improve RoCoF and frequency nadir performance. In the FFR vs. synthetic inertia comparison, the power injections for the synthetic inertia control strategy occurred much earlier compared to the FFR case, which resulted in a faster and more efficient operation to reduce the frequency nadir. The results obtained in this simulation also align well with the findings in Eriksson's report [13]. There, it was found that synthetic inertia showed better performance compared to FFR in mitigating the frequency nadir for wind turbines without speed recovery for 20% wind power production.

However, in practice, GFL inverters are rarely configured to provide synthetic inertia in island grids. This is primarily because synthetic inertia does not actively contribute to restoring the system frequency to its nominal value. As a result, the island grid would become heavily dependent on the SG to maintain frequency regulation. Should the generator underperform, synthetic inertia alone would be insufficient to stabilize the system, resulting in a blackout. Therefore, while synthetic inertia in GFL inverters appears to be more effective in mitigating disturbances, it might be less suitable for island operation. As it can be preferred to have a secondary source to maintain the frequency.

5.3 GFM

The GFM inverter was modeled as a VSM. It achieved this by emulating the swing equation that governs the active power balance between traditional SGs. A classic PI controller was used to generate the output voltage amplitude of the inverter. By doing it in this way, the VSM inherently produces synthetic inertia, and there does not have to be any dedicated control strategy for active power injection based on the RoCoF, contrary to the GFL inverter.

When analyzing the stability of the VSM with respect to frequency, it was seen that the droop constant had the most influence. After a load step increase the VSM and SG would start to oscillate against each other quickly, leading to system instability unless the droop constant of the VSM was small enough. This behavior can be explained by analyzing the Bode plot in Figure 4.24. It can be seen that the phase delay increases as the droop constant increases. This indicates that a higher droop constant produced a slower response from the inverter, leading to a more unstable system.

On the other hand, it was not evident why the oscillations between the SG and the VSM started happening for higher droop settings in the VSM. It may be a result from mismatched dynamics in speed between the fast inverter and slow SG. Since the inverter are not limited by penstocks, inertia, delays. Or that the oscillation could occur to any numerical errors.

5.4 PLL performance in strong/weak grids

From the simulations, it was observed that the overall system stability and the PLLs ability to track the grid frequency were significantly affected by the strength of the external grid and controller parameters. In the strong grid case, shown in Figure 4.5, the PLL tracked the frequency well. In the weak grid condition in Figure 4.6, the interaction between the PLL and the inverter control led to instability. This highlights that it is not the standalone performance of the PLL that becomes worse, but rather the integration with the inverter control in weak grids that causes these issues.

Upon further investigation, it was seen in 4.12 that V_q, which the PLL relies on for frequency estimation, began to oscillate as the SCC decreased. In addition, weak grids, characterized by a higher grid impedance (R and L), the injection of active power by the inverter causes a variation in the PCC voltage, as described by:

$$\Delta V_{pcc} = R \cdot i_d + \omega \cdot L \cdot i_q \tag{5.1}$$

As R and L increase, this will result in a more distorted or varying V_{pcc}, which the PLL uses as its reference voltage. Since the PLL assumes a relatively stiff voltage reference ($Vq \approx 0$) to estimate the frequency, this implies that there will be a feedback loop feeding the PLL with inaccurate data, leading to estimation errors.

When the external grid model was subject to a voltage phase angle jump, the PLL managed to track the frequency well, as long as the strength of the external grid was large enough. Initially, when the phase shift occurs, a large transient can be seen in the frequency measurement. The frequency of a signal can be calculated from the derivative of the phase angle, and therefore the transient can be seen in the measurement. When the phase angle jumps, its derivative becomes very large, resulting in a spike in the frequency measurement. The PLLs ability to track the frequency after the transient is seen to be dependent on the strength of the external grid. When the grid is stronger, the time it takes for the PLL to converge back to steady state is reduced, further emphasizing the importance of external grid strength in PLL stability.

5.5 Filtering RoCoF for system stability

In the simulations for both the external and island grid scenarios, it was observed that the system with synthetic inertia implemented led to instability for more or less all sizes of time delay and without filtering. As shown in Figure 4.17, the unfiltered RoCoF signal showed heavy oscillations and high amplitude due to high-order frequency components in the measured signal. In contrast, the filtered RoCoF measurement showed a large reduction in oscillation that leads to a more stable system. This concludes that, for a GFL synthetic inertia inverter, filtering is rather a stability requirement and that the control strategy is highly sensitive to the RoCoF measurement quality.

This conclusion also aligns well with findings reported by ENTSO-E in [11], where the importance of proper RoCoF signal processing and filtering is discussed. In their study, which included simulation results from real measurements (although type of grid is not mentioned), they compare different filtered and unfiltered RoCoF signals. Here it was shown that without filtering, the measured RoCoF reaches peaks around $\pm 2\ Hz/s$, while filtering reduced these peaks to around $\pm 0.2\ Hz/s$. Thus demonstrating the sensitivity to noise and high-frequency components that the unfiltered signals typically carry.

5.6 Sustainability and Ethics

This thesis has explored the feasibility of using GFL and GFM inverters to provide grid support, which is an important step toward enabling high penetration of RES. From a sustainability perspective, the implementation of this would reduce the dependence on fossil-fueled SGs and therefore lower emissions. In the long term, this could positively affect the public perception of IBRs and strengthen people's confidence in its reliability.

On the other hand, increased integration of GFL and GFM inverters does come with new challenges. For instance, batteries, often used as the energy source, are highly suitable from a technical perspective due to their ability to deliver rapid active power injection. However, a consequence of the growing demand for batteries leads to a complex subject regarding materials.

Life-cycle assessments indicate that batteries have a significant environmental footprint during raw material extraction and manufacturing. As discussed in [41], materials that are commonly used in battery systems, such as lithium, cobalt, and nickel, are associated with high energy and water consumption, and pose health and safety risks to miners. In the Democratic Republic of Congo, which supplies approximately 9-12% of the world's cobalt, there has been a dramatic increase in human exposure to heavy metals, as well as reports of child labor, and elevated human toxicity among workers and surrounding communities.

Although batteries do face several challenges, the concept of circular economy for batteries offers a promising path forward. In short, circular economy aims to extend the life-cycle of batteries through strategies such as remanufacturing, refurbishment, and recycling. As highlighted in [42], several countries and unions such as EU, China, USA, and Japan have already implemented regulations regarding the responsibility of battery waste and production. For example, the European Union has set targets for recovering 70% of waste batteries by 2030 and up to 90% recovery rate for elements such as nickel, copper and cobalt.

These efforts show that, while there are issues currently with extraction and production, battery handling and recycling have become growing priorities, which can also help in strengthening public confidence for the energy transition.

5.7 Future work and possibilities for improvement

This thesis has demonstrated the implementation and analysis of synthetic inertia through both GFM and GFL inverters. However, several areas remain open for future work as there were also possibilities for improvement. In the case of the GFL inverter, simulations were conducted only for PLL-based frequency measurements. Although PLLs are effective estimators in strong grid conditions, they are known to underperform in weak grids/during transients. Exploring other frequency measurements in simulation, such as the ZCD, PMU, PSP, DFT-Kalman filter, would be interesting to benchmark against the PLL.

Although the VSM control strategy was implemented in this thesis, there are several other GFM control strategies such as frequency/angle-based droop, VISMA, PSC, and augmented VSG control that are highly relevant today. A comparative study of different strategies under the same grid conditions would give a good idea of their functioning and applications.

In the simulations, the VSM demonstrated its ability to respond quickly to a frequency event. This is consistent with the theoretical capabilities of inverters, as they are not limited by mechanical delays such as the penstock, turbine inertia, and governor time constants. However, in some cases, this speed might become a drawback if an inverter responds significantly faster than the SGs, leading to oscillations between the fast and slow units. Future studies could investigate under what conditions an overly fast VSM response could lead to system instability. Additionally, testing with varying damping coefficients in the VSM high-pass filter could provide insights into optimizing stability and dynamic performance.

The synthetic inertia response was seen to react more quickly to disturbances, effectively reducing both the RoCoF and frequency nadir. Meanwhile, the FFR contributed to the restoration of the frequency back to its nominal value. Exploring hybrid control strategies that integrate both synthetic inertia and FFR to see its viability could be simulated.

6

Conclusions

This thesis has successfully implemented and analyzed the stability margins of a GFL and a GFM inverter in Matlab and Simulink. The models were tested in two different grid configurations, an island grid composed of a hydroelectric power plant and a resistive load, and connected to a larger external grid with variable impedance. The motivation for conducting this thesis work was the rapid integration of RES in power systems around the world, which makes it important to use inverters for supporting grid frequency stability. Before the models were implemented, an important distinction between control strategies used to provide synthetic inertia and FFR was established in the report. Synthetic inertia is the active power injected into the grid which is proportional to RoCoF, and FFR is the active power injected into the grid which is proportional to the frequency deviation. This definition was based on the literature review in which there was no concise definition of synthetic inertia.

During the simulations, fundamental differences were observed between the operation of GFL and GFM inverters. GFL inverters, regardless of operating mode, were found to be highly dependent on external grid strength to maintain stability. This is due to the reliance on the PLL to synchronize with the external grid. When the GFL inverter was operated in FFR mode, the stability margin was seen to decrease significantly as frequency measurement filtering increased. The delay introduced by the filtering caused the GFL inverter to inject active power after the SG in the island grid, leading to instability. When the GFL inverter was operated in synthetic inertia mode, the stability boundary depended on how the RoCoF measurement was filtered. Using a low-pass filter resulted in a linearly increasing relationship between proportional gain and filter time constant. Other filtering methods, such as moving average, could not maintain system stability other than at very small time constants. The GFM inverter, which was implemented as a VSM, was able to form its own amplitude and frequency at the PCC. The most important factor for the GFM inverter to maintain stability was found to be the regulating strength. As the droop percentage increased, the stability of the system decreased. This phenomenon was also seen through a Bode plot analysis of the emulated swing equation, as a decreasing regulating strength resulted in a greater phase delay.

The results of the simulations highlighted the real possibilities and challenges for IBRs to provide synthetic inertia in systems with low inertia. However, this work only touches the surface of a complex and evolving field and much remains to be investigated.

Bibliography

[1] O. W. in Data, *Electricity production by source*, Retrieved 2024-11-29, 2024. [Online]. Available: `https://ourworldindata.org/grapher/electricity-prod-source-stacked?country=~SWE`.

[2] P. Tielens and D. Van Hertem, "The relevance of inertia in power systems", *Renewable and Sustainable Energy Reviews*, vol. 55, pp. 999–1009, 2016, ISSN: 1364-0321. DOI: `https://doi.org/10.1016/j.rser.2015.11.016`. [Online]. Available: `https://www.sciencedirect.com/science/article/pii/S136403211501268X`.

[3] L. Dacklin, "Dynamic ffr from wind power", M.S. thesis, Chalmers Univerity of Technology, 2024.

[4] P. Energy, *Ancillary services: Definition and how they support the energy grid*, 2025. [Online]. Available: `https://www.photonenergy.pl/blog/ancillary-services`.

[5] R. H. Lasseter, Z. Chen, and D. Pattabiraman, "Grid-forming inverters: A critical asset for the power grid", *IEEE Journal of Emerging and Selected Topics in Power Electronics*, vol. 8, no. 2, pp. 925–935, 2020. DOI: `10.1109/JESTPE.2019.2959271`.

[6] Y. Li, Y. Gu, and T. C. Green, "Revisiting grid-forming and grid-following inverters: A duality theory", *IEEE Transactions on Power Systems*, vol. 37, no. 6, pp. 4541–4554, 2022. DOI: `https://doi.org/10.1109/TPWRS.2022.3151851`.

[7] J. A. Martinez-Velasco, "Introduction to electromagnetic transient analysis of power systems", in *Transient Analysis of Power Systems: Solution Techniques, Tools and Applications.* 2015, pp. 1–8. DOI: `https://doi.org/10.1002/9781118694190.ch1`.

[8] N. R. E. Laboratory, "Renewable energy grid integration: An overview of research and development needs", *National Renewable Energy Laboratory (NREL) Report*, 2020. [Online]. Available: `https://www.nrel.gov/docs/fy20osti/73856.pdf`.

[9] P. Kundur, *Power System Stability and Control.* New York: McGraw-Hill, 1994, ISBN: 978-0070359581.

[10] A. E. M. O. (AEMO), *Inertia in the nem explained*, 2023. [Online]. Available: `https://aemo.com.au/-/media/files/initiatives/engineering-framework/2023/inertia-in-the-nem-explained.pdf?la=en`.

[11] ENTSOE, *Inertia and rate of change of frequency (rocof)*, Retrieved 2025-02-06, 2020. [Online]. Available: `https://eepublicdownloads.entsoe.eu/clean-documents/SOC%20documents/Inertia%20and%20RoCoF_v17_clean.pdf`.

[12] S. kraftnät. "Snabb frekvensreserv (ffr)". Accessed:February 12, 2025. (2025), [Online]. Available: `https://www.svk.se/aktorsportalen/bidra-med-reserver/om-olika-reserver/ffr/`.

[13] R. Eriksson, N. Modig, and K. Elkington, "Synthetic inertia versus fast frequency response: A definition", *IET Renewable Power Generation*, vol. 11, no. 9, pp. 1205–1215, 2017. DOI: `10.1049/iet-rpg.2017.0370`. [Online]. Available: `https://www.researchgate.net/publication/321104126_Synthetic_inertia_versus_fast_frequency_response_a_definition`.

[14] S. Kraftnät, *Synkron kraftproduktionsmodul: Bilaga 6*, Retrieved = 2025-02-02, 2021. [Online]. Available: `https://www.svk.se/siteassets/1.om-kraftsystemet/legalt-ramverk/eu-lagstiftning/anslutningskoder/bilaga-6-provning.pdf`.

[15] P. Chen, *Frequency control process, measures and influencing factors*, 2023.

[16] L. Meng, J. Zafar, S. K. Khadem, *et al.*, "Fast frequency response from energy storage systems—a review of grid standards, projects and technical issues", *IEEE Transactions on Smart Grid*, vol. 11, no. 2, pp. 1566–1581, 2020. DOI: `10.1109/TSG.2019.2940173`.

[17] N. Modig, R. Eriksson, P. Ruokolainen, J. N. Ødegård, S. Weizenegger, and T. D. Fechtenburg, *Overview of frequency control in the nordic power system*, 2022.

[18] H. Kuisti, M. Lahtinen, M. Nilsson, *et al.*, "Nag - frequency quality report", ENTSOE, Tech. Rep., 2015.

[19] C. Wembridge, M. Davies, J. Lord, E. Franklin, S. Lyden, and M. Negnevitsky, "Fast fault-tolerant grid frequency measurement", *IEEE Open Access Journal of Power and Energy*, vol. 11, pp. 373–382, 2024. DOI: `10.1109/OAJPE.2024.3438153`.

[20] C. Wembridge, M. Davies, E. Franklin, S. Lyden, and M. Negnevitsky, "Dynamic voltage support of six-pulse bridge inverters: Equitable performance specification for future grids", in *2023 IEEE International Conference on Energy Technologies for Future Grids (ETFG)*, 2023, pp. 1–6. DOI: `10.1109/ETFG55873.2023.10407109`.

[21] *Solutions for a clean nordic energy ststem 2024 - 2030*, 2024. [Online]. Available: `https://www.statnett.no/globalassets/for-aktorer-i-kraftsystemet/utvikling-av-kraftsystemet/nordic-tso-strategy-incl.-implementation-plan---final.pdf`.

[22] T. Instruments, *Phase Locked Loop: Theory, Design, and Applications.* Texas Instruments, 2016. [Online]. Available: `https://www.ti.com.cn/cn/lit/ml/snaa106c/snaa106c.pdf`.

[23] A. Chauhan and S. K. Jain, “Frequency estimation in power systems:a brief comparison of phase locked loops and its derivatives”, in *2018 3rd IEEE International Conference on Recent Trends in Electronics, Information Communication Technology (RTEICT)*, 2018, pp. 915–919. DOI: 10.1109/RTEICT42901.2018.9012415.

[24] Y. Huang, Z. Fang, Z. He, *et al.*, “Impacts of interactions between grid-forming and grid-following converters on stability of hybrid system connected to weak grid”, in *2024 IEEE 7th International Electrical and Energy Conference (CIEEC)*, 2024, pp. 2183–2188. DOI: 10.1109/CIEEC60922.2024.10583653.

[25] D. B. Rathnayake, M. Akrami, C. Phurailatpam, *et al.*, “Grid forming inverter modeling, control, and applications”, *IEEE Access*, vol. 9, pp. 114 781–114 807, 2021. DOI: 10.1109/ACCESS.2021.3104617.

[26] G. Ying, J. Zeng, J. Song, *et al.*, “A robust phase-lock-loop for grid-following converters”, in *2024 IEEE 15th International Symposium on Power Electronics for Distributed Generation Systems (PEDG)*, 2024, pp. 1–5. DOI: 10.1109/PEDG61800.2024.10667404.

[27] X. Gao, D. Zhou, A. Anvari-Moghaddam, and F. Blaabjerg, “Seamless transitions between grid-following and grid-forming control: A novel switching method”, in *2023 11th International Conference on Power Electronics and ECCE Asia (ICPE 2023 - ECCE Asia)*, 2023, pp. 1154–1160. DOI: 10.23919/ICPE2023-ECCEAsia54778.2023.10213821.

[28] J. Fang, J. Liu, H. Wu, J. Chen, and F. Blaabjerg, *Grid-Forming Converters : Principles, Control, and Applications in Modern Power Systems.* Chantilly : Elsevier Science Technology, 2024, 2024.

[29] W. Binbing, X. Abuduwayiti, C. Yuxi, and T. Yizhi, “Rocof droop control of pmsg-based wind turbines for system inertia response rapidly”, *IEEE Access*, vol. 8, pp. 181 154–181 162, 2020. DOI: 10.1109/ACCESS.2020.3027740.

[30] J. Roldán-Pérez, M. Prodanovic, and A. Rodríguez-Cabero, “Detailed discrete-time implementation of a battery-supported synchronverter for weak grids”, in *IECON 2017 - 43rd Annual Conference of the IEEE Industrial Electronics Society*, 2017, pp. 1083–1088. DOI: 10.1109/IECON.2017.8216186.

[31] C. Ekstrand, E. Götenfelt, S. Johansson, and D. V. Alba, “Black start of microgrid with an energy storage”, Chalmers Univeristy of Technology, Tech. Rep., 2021.

[32] R. Teodorescu, M. Liserre, and P. Rodriguez, *Grid Converters for Photovoltaic and Wind Power Systems.* Wiley-IEEE Press, 2007, p. 416, ISBN: 978-0-471-94571-5. [Online]. Available: https://ieeexplore.ieee.org/document/4360209.

[33] Y. Zhou, P. Huang, and F. Blaabjerg, “Synchronous reference frame-based control for grid-connected renewable energy systems”, *IEEE Transactions on Industry Applications*, vol. 47, no. 2, pp. 984–994, 2011. DOI: `10.1109/TIA.2010.2102732`. [Online]. Available: `https://ieeexplore.ieee.org/document/5619968`.

[34] L. Harnefors and H.-P. Nee, *Model-based current control of ac machines using the internal model control method*, Accessed: 2025-02-26, 1998. [Online]. Available: `https://ieeexplore.ieee.org/stamp/stamp.jsp?arnumber=658735`.

[35] MathWorks, *Choose a solver*, Accessed: 2025-02-26, 2025. [Online]. Available: `https://se.mathworks.com/help/simulink/ug/choose-a-solver.html`.

[36] MathWorks, *Three-phase programmable voltage source*, Accessed: 2025-03-04. [Online]. Available: `https://se.mathworks.com/help/sps/powersys/ref/threephaseprogrammablevoltagesource.html`.

[37] Energimarknadsinspektionen, *Eifs 2018:2 – energimarknadsinspektionens föreskrifter om fastställande av generellt tillämpliga krav för nätanslutning av generatorer*, Föreskrift, 2018. [Online]. Available: `https://ei.se/om-oss/publikationer/publikationer/foreskrifter-el/2018/foreskrift-eifs-20182`.

[38] N. E. S. O. (ESO), “Sub-synchronous oscillations: Risk management in a changing power system”, *National Grid ESO Technical Report*, 2023. [Online]. Available: `https://www.neso.energy/document/319056/download`.

[39] C. S. C. B4, “Guidelines for subsynchronous oscillation studies in power electronics dominated power systems”, CIGRÉ, Tech. Rep. Technical Brochure 909, 2023. [Online]. Available: `https://electra.cigre.org/329-august-2023/technical-brochures/guidelines-for-subsynchronous-oscillation-studies-in-power-electronics-dominated-power-systems.html`.

[40] X. Xie, J. Li, S. Wang, L. Zhang, and Z. Chen, “Analysis of ultra-low frequency oscillations in weak ac grids with hydraulic generation”, *International Journal of Electrical Power & Energy Systems*, vol. 155, p. 109 553, 2024. DOI: `10.1016/j.ijepes.2023.109553`. [Online]. Available: `https://doi.org/10.1016/j.ijepes.2023.109553`.

[41] J. Porzio and C. D. Scown, *Life-cycle assessment considerations for batteries and battery materials*, *, n.d. [Online]. Available: `https://www.nature.com/articles/s41560-021-00934-2`.

[42] M. Goyal, K. Singh, and N. Bhatnagar, *Circular economy conceptualization for lithium-ion batteries: Material procurement and disposal process*, Department of Chemistry and Department of Electronics and Communication Engineering, Manipal University Jaipur, India, 2023.

DEPARTMENT OF SOME SUBJECT OR TECHNOLOGY
CHALMERS UNIVERSITY OF TECHNOLOGY
Gothenburg, Sweden
www.chalmers.se

CHALMERS
UNIVERSITY OF TECHNOLOGY